Biophysical Journal Volume 106 April 2014 1811–1821

Attraction of Rotors to the Pulmonary Veins in Paroxysmal Atrial Fibrillation: A Modeling Study

Conrado J. Calvo,[†‡§] Makarand Deo,[†¶] Sharon Zlochiver,[†||] José Millet,[‡§] and Omer Berenfeld[†***]

[†]Center for Arrhythmia Research, Department of Internal Medicine, and Department of Biomedical Engineering, University of Michigan, Ann Arbor, Michigan; [‡]BioITACA Grupo de Bioingeniería, Instituto de Aplicaciones Avanzadas, Valencia, Spain; [§]Departamento Ingeniería Electrónica, Universitat Politècnica de Valencia, Valencia, Spain; [¶]Department of Engineering, Norfolk State University, Norfolk, Virginia; [||]Department of Biomedical Engineering, Tel Aviv University, Ramat Aviv, Israel; and **Department of Biomedical Engineering, University of Michigan, Ann Arbor, Michigan

ABSTRACT Maintenance of paroxysmal atrial fibrillation (AF) by fast rotors in the left atrium (LA) or at the pulmonary veins (PVs) is not fully understood. To gain insight into this dynamic and complex process, we studied the role of the heterogeneous distribution of transmembrane currents in the PVs and LA junction (PV-LAJ) in the localization of rotors in the PVs. We also investigated whether simple pacing protocols could be used to predict rotor drift in the PV-LAJ. Experimentally observed heterogeneities in I_{K1}, I_{Ks}, I_{Kr}, I_{to}, and I_{CaL} in the PV-LAJ were incorporated into two- and pseudo three-dimensional models of Courtemanche-Ramirez-Nattel-Kneller human atrial kinetics to simulate various conditions and investigate rotor drifting mechanisms. Spatial gradients in the currents resulted in shorter action potential duration, minimum diastolic potential that was less negative, and slower upstroke and conduction velocity for rotors in the PV region than in the LA. Rotors under such conditions drifted toward the PV and stabilized at the shortest action potential duration and less-excitable region, consistent with drift direction under intercellular coupling heterogeneities and regardless of the geometrical constraint in the PVs. Simulations with various I_{K1} gradient conditions and current-voltage relationships substantiated its major role in the rotor drift. In our 1:1 pacing protocol, we found that among various action potential properties, only the minimum diastolic potential gradient was a rate-independent predictor of rotor drift direction. Consistent with experimental and clinical AF studies, simulations in an electrophysiologically heterogeneous model of the PV-LAJ showed rotor attraction toward the PV. Our simulations suggest that I_{K1} heterogeneity is dominant compared to other currents in determining the drift direction through its impact on the excitability gradient. These results provide a believed novel framework for understanding the complex dynamics of rotors in AF.

INTRODUCTION

The mechanisms of atrial fibrillation (AF), the most common cardiac arrhythmia in the clinical practice, are not fully understood. Acute AF in normal isolated sheep hearts has been found to often depend on fast rotors localized mainly to the posterior wall of the left atrium (LA) and the pulmonary-veins (PVs) junction (PV-LAJ) with fibrillatory conduction toward the rest of the atria (1). Recent clinical data also point to rotors in various atrial sites as a mechanism driving paroxysmal AF (2–4). Previous simulations have already demonstrated that rotors can occur in the PV-LAJ, provided the PV size is adequate and that nonuniform coupling conditions exist (5). However, how the rotors form or drift in the PV-LAJ, as well as the underlying ionic mechanisms, have not been investigated systematically (6,7).

Earlier studies using simplified cardiac models have shown a causal link between rotor drift and spatial heterogeneity in the action potential (AP) properties (8). Rotors drifted toward regions with prolonged action potential duration (APD) or reduced excitability (9), which were mainly due to heterogeneities in multiple ion channels (10). In particular, the role of K^+ currents I_{K1} (inward rectifier potassium current) and I_{Kr} (rapid delayed rectifier potassium current) may be important, because they are known to be heterogeneously distributed in the heart (11), and have also been shown to influence rotor dynamics by affecting both the membrane APD and excitability (12–14). However, the complex heterogeneity in the expression of these channels at the PV-LAJ, such as in dogs, which show a larger current density of I_{Kr} and a smaller density of I_{K1} in the PV compared to LA (15,16), in conjunction with structural discontinuities (i.e., narrow PV sleeves compared to the larger LA), precludes a simple prediction of the rotor dynamics at the PV-LAJ.

Our study aims to elucidate ionic mechanisms of rotor drifting at the PV-LAJ. We construct two- and pseudo three-dimensional models of the PV-LAJ to investigate the hypothesis that the characteristic heterogeneous dispersion of transmembrane currents during paroxysmal AF, in absence of remodeling, is a determinant of rotor drift. Our numerical simulations demonstrate I_{K1} dominance in conveying a preferential rotor drift direction toward the PVs. We further demonstrate the cycle-by-cycle mechanism by which regions with longer refractoriness and lower excitability tend to attract rotors, and propose a set of measures to confirm our mechanistic proposition linking the ionic properties of the atrial substrate and the predisposition of the

---

Submitted October 1, 2013, and accepted for publication February 25, 2014.

*Correspondence: oberen@umich.edu

Editor: Andrew McCulloch.

0006-3495/14/04/1811/11 $2.00

CrossMark

http://dx.doi.org/10.1016/j.bpj.2014.02.030

PVs, or any other region, to attract or repel rotor activity during AF (17–19).

METHODS

Numerical models

Numerical simulations were performed on three models of the junction between the LA and the PV (see Fig. 1 and the Supporting Material) with increasingly realistic anatomical descriptions, as follows:

1. A 50 × 50 mm^2 regular two-dimensional square mesh model was implemented and subjected to no-flux boundary conditions;
2. A pseudo-three-dimensional cylindrical surface model was constructed by applying no-flux boundary conditions at the LA and PV edges, and periodic boundary conditions on the other two edges of a regular two-dimensional mesh; and
3. A pseudo-three-dimensional funnel-shaped surface was constructed with near-equilateral triangulated mesh with no-flux boundary conditions on the wide (LA) and narrow (PV) edges.

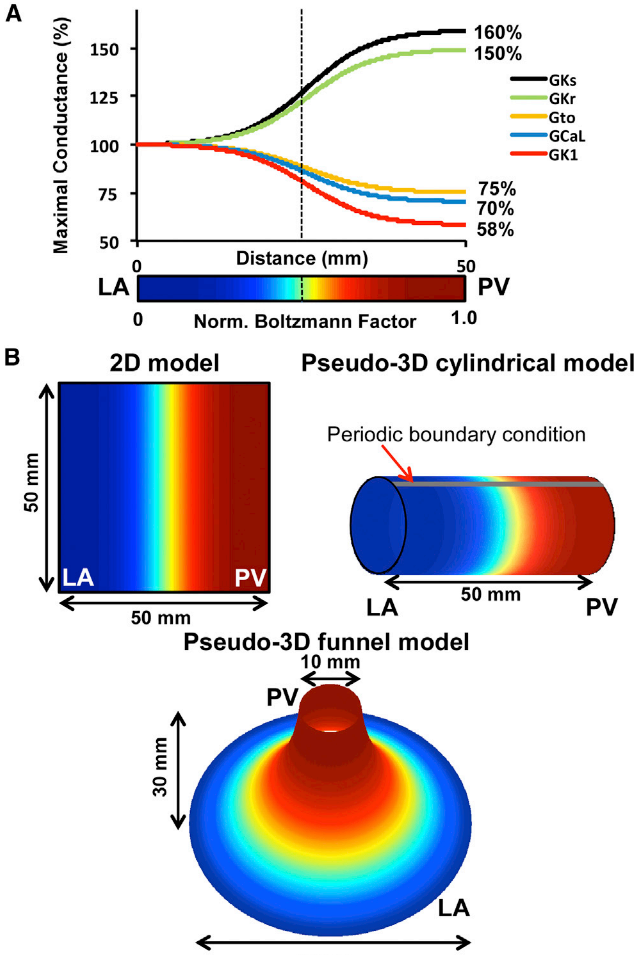

FIGURE 1 The PV-LAJ models. (*A*) Conductances for I_{CaL}, I_{kr}, I_{ks}, I_{to}, and I_{K1} follow a Boltzmann function ($x_{1/2}$ = 25 mm, *vertical dashed line*; $\Delta x = 5$ mm) from LA to PV. (*Color bar*) Normalized Boltzmann factor across the junction. (*B*) Simulations were performed on 1), two-dimensional model of 50 × 50 mm^2; 2), cylindrical pseudo three-dimensional model generated by a periodic boundary condition in the two-dimensional model; and 3), a funnel-shaped pseudo three-dimensional model. Colors represent the Boltzmann factor values. (*Cyan-yellow*) Steepest gradient region in the PV-LAJ.

The transmembrane potential was based on the Courtemanche-Ramirez-Nattel and Kneller (CRN-K) model of human atrial cell kinetics in the presence of 0.0015 μM acetylcholine (20–22). Electrical activity was computed using a mono-domain and numerically stable Euler forward scheme with 100-μm internodal distance, 0.005-ms time step, and isotropic diffusion coefficient of 0.062 mm^2/ms adjusted for conduction velocity of 48 cm/s. Initial conditions were the steady-state membrane variables after pacing a single cell at 1 Hz for 10 s.

Heterogeneous ionic conditions were implemented by assigning a spatial Boltzmann distribution of conductance for I_{K1}, I_{Ks} (slow delayed rectifier potassium current), I_{Kr}, I_{to} (outward transient potassium current), and I_{CaL} (L-type calcium current) values between the LA and the PV based on data from dogs (16). This is described in Fig. 1 *A*, where maximum conductance for I_{Kr} and I_{ks} were increased by 50 and 60%, respectively, whereas I_{K1}, I_{to}, and I_{CaL} were diminished by 42, 25, and 30%, respectively. Three conditions of ionic heterogeneity were modeled, as follows:

Condition I—all currents varied spatially according to their corresponding Boltzmann function;
Condition II—all currents, except I_{K1}, varied; and
Condition III—only I_{K1} varied in space.

Additional conditions of heterogeneous intercellular coupling coefficient and distribution of I_{Na} (sodium current) are described and studied in the Supporting Material. Reentrant excitation patterns were induced by S1-S2 cross-field stimulation protocols and their pivoting points were identified as a singularity point (SP) and tracked in the phase domain (see Fig. S1 and Movie S1 in the Supporting Material).

Effective refractory period (ERP) was defined as the shortest interval of premature excitation for various basic cycle length trains after reaching steady state (see the Supporting Material). Spatial profiles of APD and peak sodium channels availability $(h \times j)_{peak}$ were obtained by averaging those parameters in time for every pixel across the model in the last two 5-s simulations. Measurements of minimum diastolic potential (MDP) and maximum upstroke velocity (dV/dt_{max}) followed a similar procedure.

RESULTS

Ionic gradients and rotor attraction toward the PV

As a demonstration of dependence of rotor drift in the PV-LAJ on the specific ionic current heterogeneity, we generated rotors in the three conditions implemented in the cylindrical and flat model and tracked the spontaneous trajectory of their SP. Fig. 2 demonstrates that the rotor in the heterogeneous PV-LAJ region is unstable and its drift direction is a direct consequence of the particular ionic dispersion.

In Condition I, i.e., heterogeneity in the currents I_{K1}, I_{Ks}, I_{Kr}, I_{to}, and I_{CaL} as characterized at the PV-LAJ in dog (16), the drift is toward the PV edge of the model. However, when all the currents except I_{K1} are set to be heterogeneous, and I_{K1} density is maintained homogenously, and is equal to the LA region value (Condition II), the drift reverses toward the LA (note that when the I_{K1} is homogeneously equal to the PV region—which is not shown here—the drift is also toward the LA). On the other hand, when all the currents are set uniform (either with the LA or the PV values) and only I_{K1} is set to disperse as in the dog (Condition III),

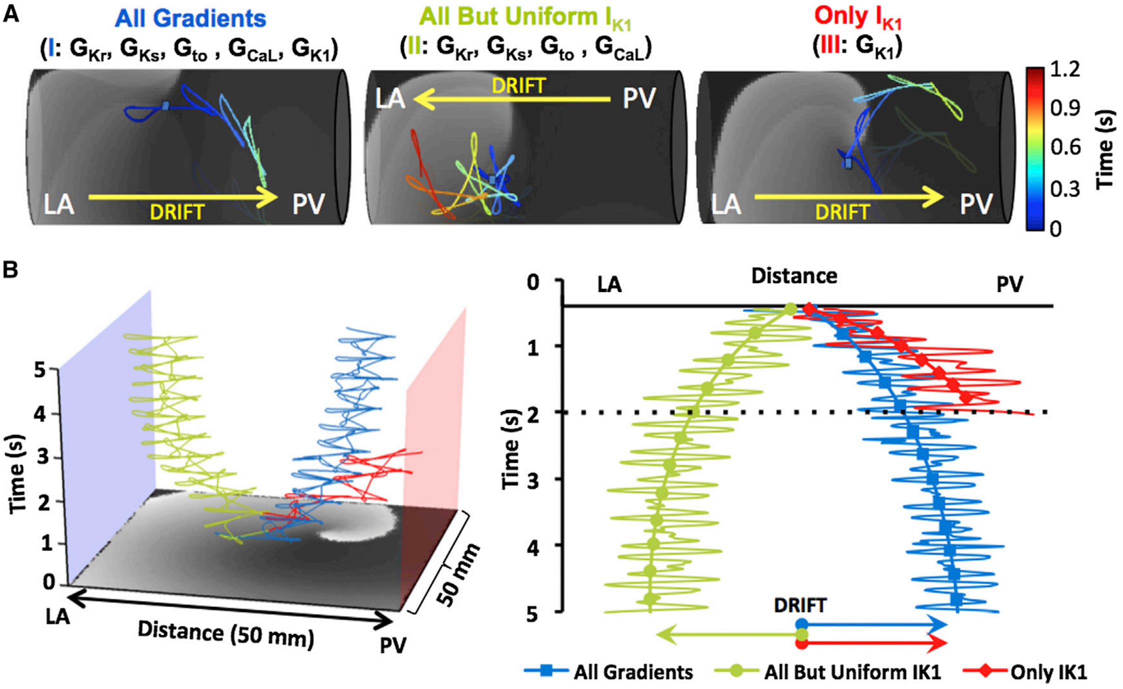

FIGURE 2 Simulations of rotor drift in the PV-LAJ and I_{K1} role. (*A*) Rotor dynamics on the cylindrical model using the CRN-K kinetics under three conditions: 1), all currents varied spatially; 2), all currents varied spatially, except I_{K1}; 3), only I_{K1} varied spatially. (*Color-coded traces*) SP trajectory of rotors initiated at the middle of the models (*blue dots*). Rotors under Conditions I and III drifted toward the PV edge. Drift direction was reversed when I_{K1} heterogeneity was excluded in Condition II. (*B*) Time-space plots (and *arrows*) show rotor drift for the three conditions in a flat two-dimensional model.

the drift is again toward the PV, but with a faster rate as compared with the drift in Condition I. This set of three scenarios in cylindrical as well as in the flat models, shown in Fig. 2, clearly points to the strong effect of I_{K1} on the direction of the rotor drift in the LA-PV junction area.

As controls, we simulated rotors in two-dimensional models with uniform ionic properties of either the LA or the PV that revealed nondrifting rotors. The rotors in the model with uniform LA properties were slightly faster than those in the model with the uniform PV properties (7.7 vs. 7 Hz, respectively; other properties of the rotors did not vary by >~10%; see Fig. S2). We further tested the effect of all individual and pairwise currents on drift by switching them from heterogeneous to uniform (see Fig. S3) and concluded again that the I_{K1} heterogeneity is the primary ionic factor that determines the direction of the drift toward the PV. To better understand the mechanisms leading to the attraction of the rotor toward the PV region, we quantified electrophysiological properties of the action potential and its propagation across the PV-LAJ.

Heterogeneous excitability and rotor drift in the PV-LAJ

Ionic heterogeneity is imposing nonuniform excitability properties and a rotor drift toward a predictable direction (9). In Fig. 3, we analyze the role of tissue excitability in rotor drifts by quantifying the spatio-temporal distribution of the product of membrane model parameters *h* and *j* ($h \times j$, the fraction of sodium channels available for activation), which determines the I_{Na} availability during rotor pivoting (22). Fig. 3 *A* illustrates the drift trajectory of a rotor in a two-dimensional model under Condition I and shows a time-space plot of $h \times j$ along the line of the drift. A closer look at the time-space plot near the pivoting location during a single cycle shows higher values of $h \times j$ at the left side (LA) of the drift than at the right side (PV). Thus, a progressive shift of the pivoting point toward the PV is always toward a region with lower $h \times j$ values.

Fig. 3 *B* shows snapshots of the voltage and $h \times j$ at a moment when the wavefront near the rotor tip is propagating toward the LA (*top*) and a half-cycle later, when that wavefront is propagating toward the PV (*bottom*). The $h \times j$ snapshots clearly demonstrate that the wave propagating toward the LA is facing a higher $h \times j$ (*red*) as compared with the wave propagating toward the PV. The $h \times j$ gradient during the drift is further confirmed by plotting the time-course of the voltage and $h \times j$ at 2 pixels flanking momentarily the SP of the rotor: one on the LA side and the other on the PV side, 4 mm away from the tip. Those plots show that the peak $h \times j$ for each cycle at the LA side is always >0.4 and at the PV side is always <0.4. As illustrated in greater detail in Fig. S4, the alternating SP drift is larger during propagation toward the PV (low $h \times j$) than during its propagation toward the LA (high $h \times j$). The result is a net drift toward the lower $h \times j$ (i.e., less

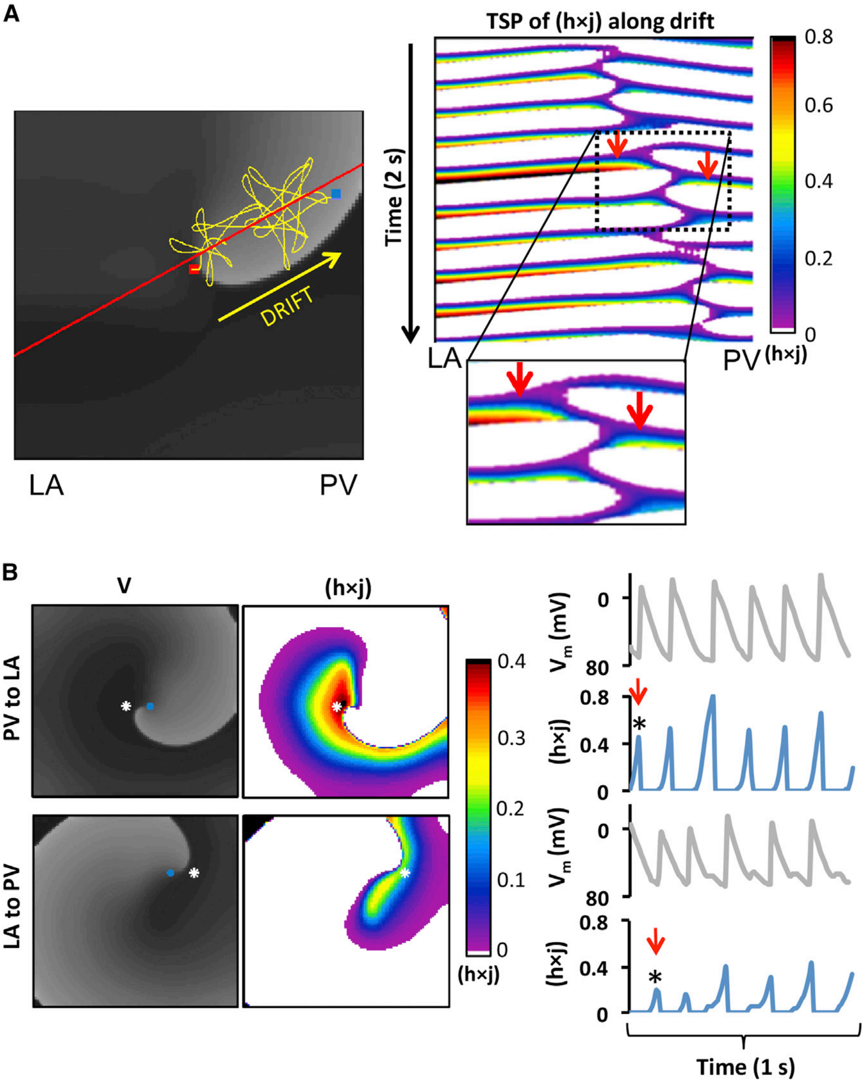

FIGURE 3 Heterogeneous sodium availability during rotor drift. (*A*) (*Left*) Voltage snapshot (*gray scale*) with superimposed trajectory of rotor SP (*yellow tracing*) drifting from the center of the model (*red dot*) toward its final location at the PV edge (*blue dot*). (*Right*) Color-coded time-space plot for $h \times j$ along the rotor drift direction (*red solid line* in voltage snapshot). (*Inset*) Magnified view showing close to the rotor core $h \times j$ is larger on the LA side than on the PV side (*red arrows*). (*B*) (*Left*) Snapshots of voltage (*gray scale*) and $h \times j$ (*color-coded*) maps at two instances; when the rotor wave-front near the core is directed from PV to LA (*top*); and approximately a half-cycle later, when it is directed from LA to PV (*bottom*). (*Blue dots*) Tip of the rotor; (*white dots*) 4 mm from tip, toward LA (*top*) and toward PV (*bottom*). (*Right*) Single-pixel time-series showing simultaneous voltage and $h \times j$ (*white dots*). (*Red arrows*) Times of the voltage and $h \times j$ snapshots on the left side of the panel.

excitable) region. Importantly, it is noticeable that a presence of heterogeneity at the core area is critical for the rotor drift; in absence of heterogeneity at the core, a rotor may be stable (see Fig. S5).

Fig. 4 summarizes the relationship between rotor drift and spatial distribution of excitability factors during reentry in the three conditions simulated. Fig. 4 *A* shows, for illustration purposes, a map with the distribution of the time-averaged $h \times j_{\text{peak}}$ for the model with greatest excitability gradient (Condition III) and shows that those values are approximately twofold larger in the LA edge compared with those at the PV edge (0.8 and 0.4, respectively). The graph in Fig. 4 *A* presents the spatial profiles of the $h \times j$ and the drift direction for the three conditions. It is seen that the two conditions with lowest density of I_{K1} at the PV edge (*blue* and *red*) have profiles with reduced $h \times j$ at that edge as well, in contrast to the condition without the I_{K1} gradient, where $h \times j$ is maximal at the PV edge. Overall, the directionality of the drift in the three conditions as indicated by the superimposed arrows is fully consistent with the rotor attraction by any region with lowest $h \times j$ values.

Next, Fig. 4 *B* quantifies metrics associated with the AP measurements of excitability: we focus on the $dV/dt_{\max}$ and MDP, which plays a role in determining the availability of I_{Na} during the membrane depolarization. On the left side, we present samples of aligned pairs of action potentials recorded in locations (*asterisks*) near the LA (*red*) and PV (*blue*) edges during reentry in the three conditions. As can be appreciated, each condition presents a distinct heterogeneity in its action potentials as quantified on the right side of the panel. For the three conditions, the drift direction is toward the regions with lowest excitability, as determined by the slowest $dV/dt_{\max}$ and most positive MDP (22).

Pacing predictors of rotor drift in the PV-LAJ

We investigated pacing protocols that could be used to predict drift direction. In Fig. 5, we demonstrate APD profiles

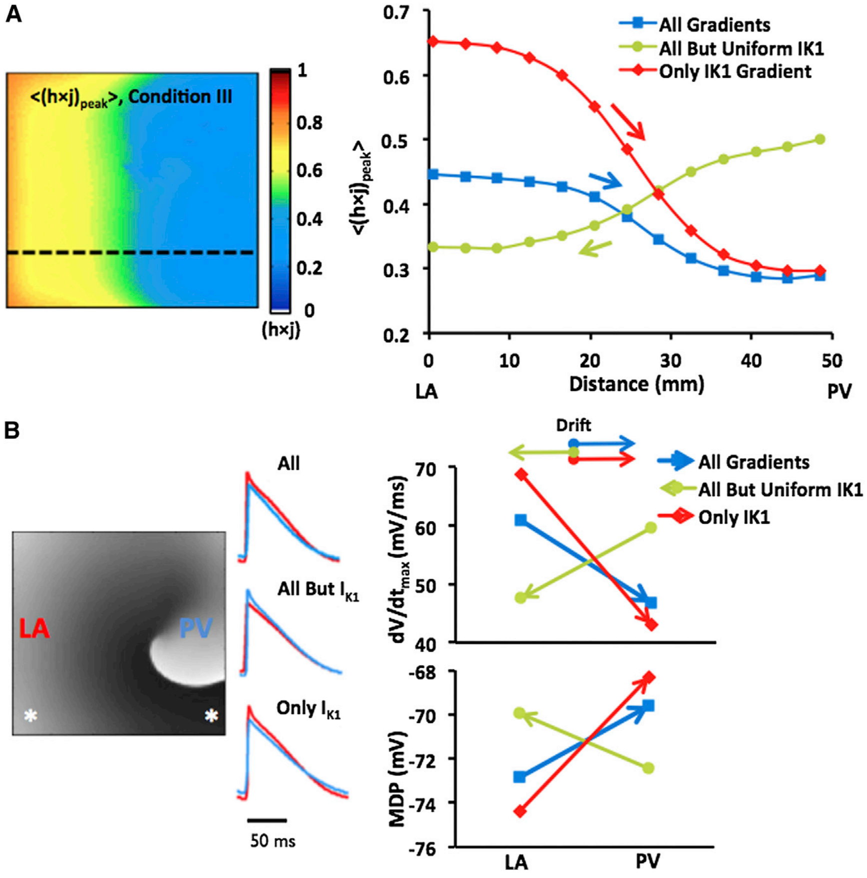

FIGURE 4 Gradients of sodium availability and AP measurements during rotor drift predict drift direction. (*A*) (*Left*) Map of averaged $(h \times j)_{peak}$ ($\langle (h \times j)_{peak} \rangle$) during rotor activity under Condition III; only I_{K1} is showing an LA-to-PV decrease. (*A*) (*Right*) PV-LAJ spatial profiles of $\langle (h \times j)_{peak} \rangle$ for the three conditions modeled. (*Superimposed arrows*) Direction of rotor drift for each condition, consistently toward the region of lowest $\langle (h \times j)_{peak} \rangle$ (lowest sodium availability). (*B*) AP measurements of excitability during reentry. (*Left*) A voltage snapshot and APs from the LA (*red*) and PV (*blue*) edges (*asterisks* on *map*) for the three conditions simulated. (*Right*) Upstroke velocity (dV/dt_{max}) and MDP at the LA and PV region with direction of drift (*arrows*) for the three conditions. Drift is consistently toward lowest upstroke velocity and most positive MDP regions.

consequential of a steady pacing at the center of the junction where rotors were initiated and radial propagation. Fig. 5 *A*, illustrates the steady-state APD_{80} profiles at 2 Hz pacing for the three conditions along with an indication of drift direction. The APD profiles show different gradients for each particular condition of ionic gradients. Correlating the APD profiles with the reentry simulations we find that rotors initiated in Condition I drifted toward the PV (Fig. 2 *B*) and stabilized at the shortest APD region. When the I_{K1} gradient is excluded (Condition II), the APD difference across the transition is maintained, but the drift direction reversed. In Condition III, the spatial APD difference is reversed. Yet, the rotor drifts from the LA to the PV, and does it even faster (Fig. 2 *B*) because there are no ionic effects opposing the I_{K1} effect. Fig. 2 *B* presents ERP and dV/dt_{max} determined at 2 Hz pacing at the LA and PV edges. It is demonstrated that while ERP is, like APD_{80}, inconsistent with drift toward either longer or shorter periods, the drift is consistently toward the highest dV/dt_{max} for the three conditions.

Noticeably, the LA-PV dV/dt_{max} gradient directions (measured at 2 Hz pacing) in Fig. 5 *B* are contrasting the dV/dt_{max} gradient directions in Fig. 4 *B* (measured during reentry at ~7 Hz), leading us to further assess the dependency of AP properties on pacing frequency. The traces at the top of Fig. 5 *C* show that APs in Condition I display distinct variation of duration at different repolarization levels during increasing pacing rate from 2 to 7 Hz. The bar-graph at the bottom of Fig. 5 *C* compares APD values across Condition I for 1000, 500, and 140 ms cycle lengths (respectively, 1, 2, and 7.14 Hz pacing rates). It shows that at 1 Hz pacing, the PV APD is shorter than the LA at all repolarization levels; and that at 2 Hz, and even more so at 7 Hz (close to the rotor frequency), APD_{90} at the PV edge is longer than in the LA. Fig. 5 *D* shows that APD_{80}, dV/dt_{max}, and ERP across the model with Condition I heterogeneity measured only at a cycle lengths of 140 ms (7.14 Hz) resulted in gradient directions consistent with the previous prediction of the drift toward longer APD and lower excitability (9,23,24). However, the LA-PV dispersion of MDP displayed a rate-independent correlation with the drift direction. Regardless of the pacing rate, though, the drift was found consistently toward the region with the most positive MDP (also for Conditions II and III, not shown).

The I_{K1} and rotor drift direction

Fig. 2 and Fig. S3 demonstrated the important role of I_{K1} in determining the direction of the rotor drift in the PV-LAJ. Here we study the effect of various relevant current-voltage relationships of I_{K1} on such drift direction. Fig. 6 *A* shows four relationships between the current density and transmembrane voltage (I/V relationship) for different I_{K1}

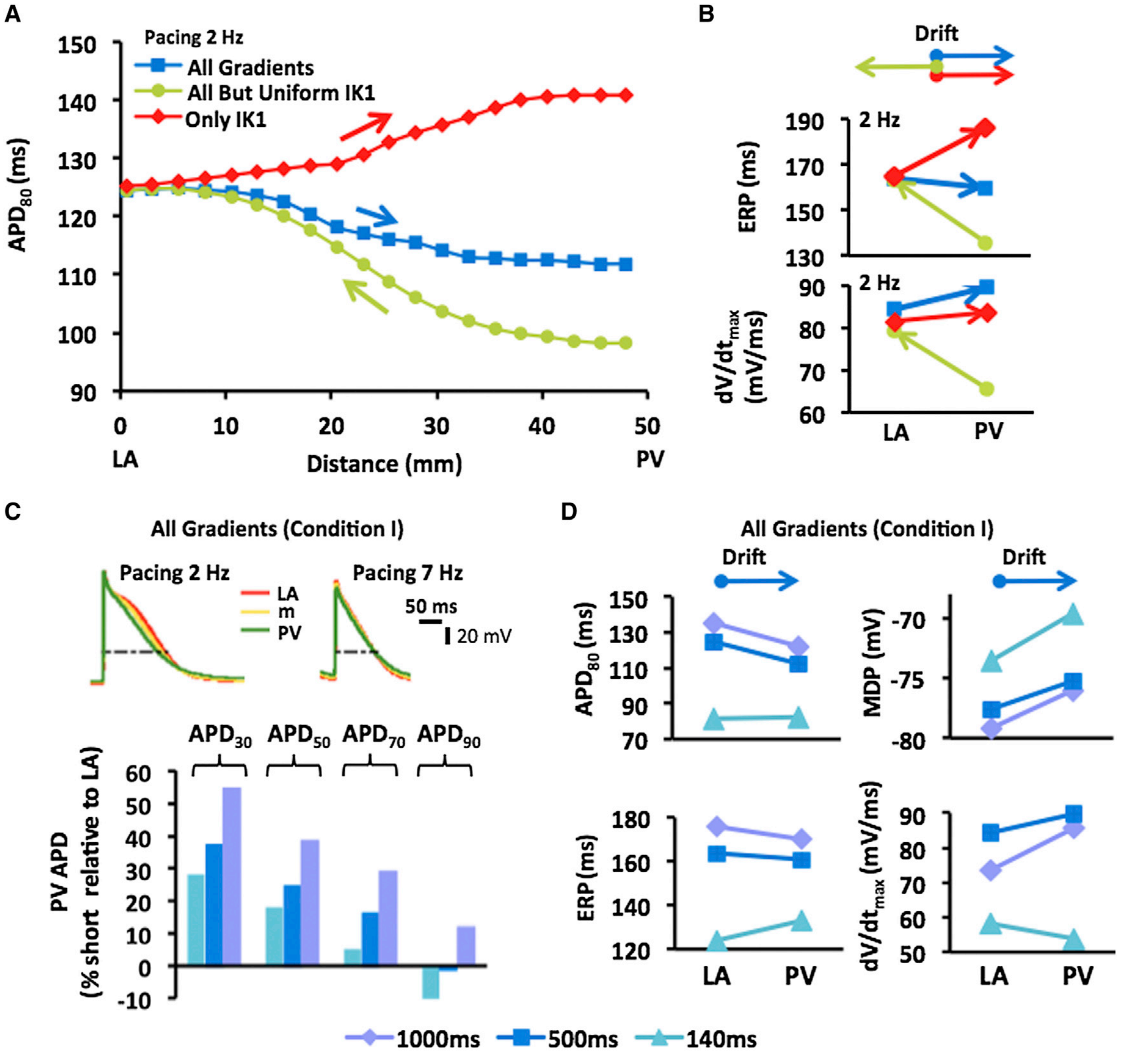

FIGURE 5 Pacing predictors for drift direction. (*A*) APD_{80} profiles resulting from pacing at 2 Hz in the middle of the model show inconsistent drift (*arrows*) toward either short or long APD regions for the three simulated conditions. (*B*) ERP and dV/dt_{max} measured at LA and PV at 2 Hz pacing for the three conditions show inconsistent drift direction. (*C*) Frequency-dependence of APDs. (*Top*) Single pixels APs in three locations across the PV-LAJ at 2- and 7-Hz pacing. (*Bottom*) APDs in the PV relative to those in the LA. Notably, at all pacing rates slower than 140 ms (7.14 Hz, close to the rotation frequencies in the LA and PV; see Fig. S1), the APD in the PV is shorter than in the LA (except APD_{90} at 140 and 500 ms). (*D*) APD_{80}, ERP, MDP, and dV/dt_{max} in the LA and PV as measured at 1000, 500, and 140 ms pacing rate. Drift direction is also indicated (*arrows* on *top*). To see this figure in color, go online.

levels, including up- and downregulation, as well as their corresponding APs showing different APDs and MDPs. The four I/V relationships were incorporated in a PV-LAJ model with Condition I, and rotor activity as well as AP parameters were tracked. As can be observed from Fig. 6 *B*, increasing or decreasing the $I_{K1,}$ increases or decreases the average rotor frequency, respectively. Fig. 6 *C* demonstrates that $h \times j$ profiles across the PV-LAJ vary both in levels and gradient directions as a consequence of altering the I/V relationships. In particular, it is noticeable that the rotor drifts toward the PV for a broad range of I_{K1} levels whereas a reversal in the drift and $h \times j$ gradient direction occurs only at a 75% reduction in I_{K1} (a behavior similar to that of a uniform I_{K1} shown under Condition II in Fig. 2).

Up- and downregulation of I_{K1} also hyperpolarize and depolarize MDP as well as increase and decrease upstroke speed, respectively (Fig. 2 *D*), with consistent drifts toward higher MDP and lower upstroke velocity. Overall, the consequences of altering the I/V properties of I_{K1} in the heterogeneous models on, MDP and upstroke velocity shown in Fig. 2, *C* and *D*, are complex and suggest a nonmonotonic dependency. Nevertheless, further alterations in extracellular potassium concentration in the range of 4–7 mM, as well as alteration in the I/V profile to resemble closely those of $Kir_{2.1}$ or $Kir_{2.3}$ (25), affect excitability and rotation frequency, but do not alter direction of $h \times j$ gradients and drift directions toward the PV (see Fig. S6).

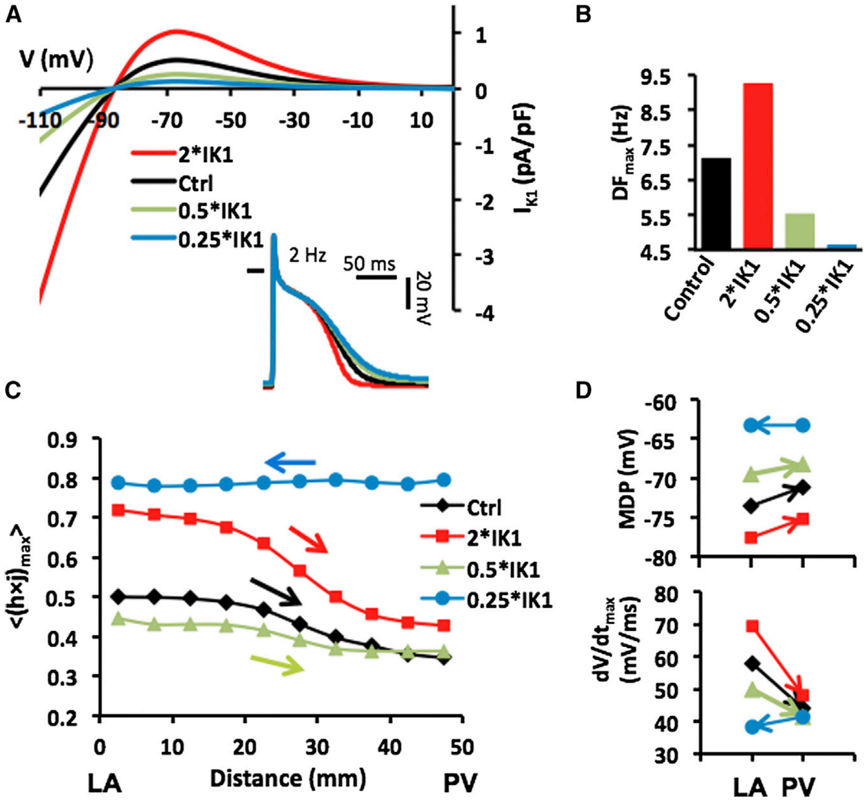

FIGURE 6 I_{K1} levels and drift direction. (*A*) I_{K1} I/V curves for normal (control) and other levels of I_{K1} density. Steady-state APs induced at 2 Hz are illustrated. (*B*) Rotation frequency in LA homogenous model for each I_{K1} density level. (*C*) Average peak I_{Na} availability profiles show drift toward lower excitability (*arrows*) in a model with Condition I. (*D*) Analysis of MDP and dV/dt_{max} for each profile at single pixels in the LA and PV (4 mm from boundaries) under Condition I. To see this figure in color, go online.

Comparative effects of ionic, passive, and geometrical gradients on rotor drift

A gradient in membrane currents is just one of the factors that may affect rotor drift. For example, the PV-LAJ is known to have a heterogeneous intercellular coupling that is also known to affect rotor drifts. Based on a 25% lower density of gap junctions and connexins relative to the rest of the atria (26), the intercellular coupling in the PVs' region of the LA is speculated to be lower than that of the LA. As expected, the gradient in the passive properties of the tissue (24,27) attracted the rotor toward the PV, where the coupling coefficient is the lowest (see Fig. S7) and in a direction similar to that of the ionic gradients. Interestingly, our simulations suggest that the I_{K1} heterogeneity is still a major factor determining the drift direction in the presence of the heterogeneous intercellular coupling.

In addition to the ionic heterogeneity, a prominent geometrical feature of the LA-PV junction, namely its funnel-shaped walls, may also affect functional rotor dynamics by spatial confinement in the PV and asymmetric source-sink relationships with the LA (5). In contrast to the gradient in the coupling, the effect of the geometrical confinement of the PVs on drift is not clear. Accordingly, we constructed a control homogeneous model with a uniform level of ionic currents and another model with heterogeneous distribution of the ionic currents (Figs. 1 and 2). A single functional rotor was initiated in both models close to the LA edge (see Fig. S1) and its spontaneous meandering and drift were tracked by the trajectory of its SP. In Fig. 7 we show that the ionic gradients play an important role in the drift of a rotor toward the PV even in the presence of a constraint imposed by the narrowing space near the PV. Panel *A* shows phase snapshots and the trajectory of the rotor superimposed on a homogeneous (*left*) and heterogeneous (*right*) funnel models. Panel *B* is a bull-eye presentation of the rotor trajectory in the homogeneous (*left*) and heterogeneous (*right*) funnel models. Panel *C* of Fig. 7 shows that the SP trajectory over a period of 5 s after onset in the heterogeneous versus the homogeneous model is characterized by a drift toward the PV, with gradual shortening of the distance between the pivoting point and the PV edge of the funnel model. Thus, we conclude that a generic funnel shape of a realistic dimension of the LA-PV junction does not eliminate the rotor attraction of the PV that is induced by the dispersion of ionic currents across that region.

DISCUSSION

The main findings of our study are as follows:

1. The heterogeneous distribution of transmembrane currents in the PV-LAJ plays a major role in the preferential localization of rotors near or at the PVs, and that the spatial dispersion of I_{K1} is particularly important in determining such attraction.

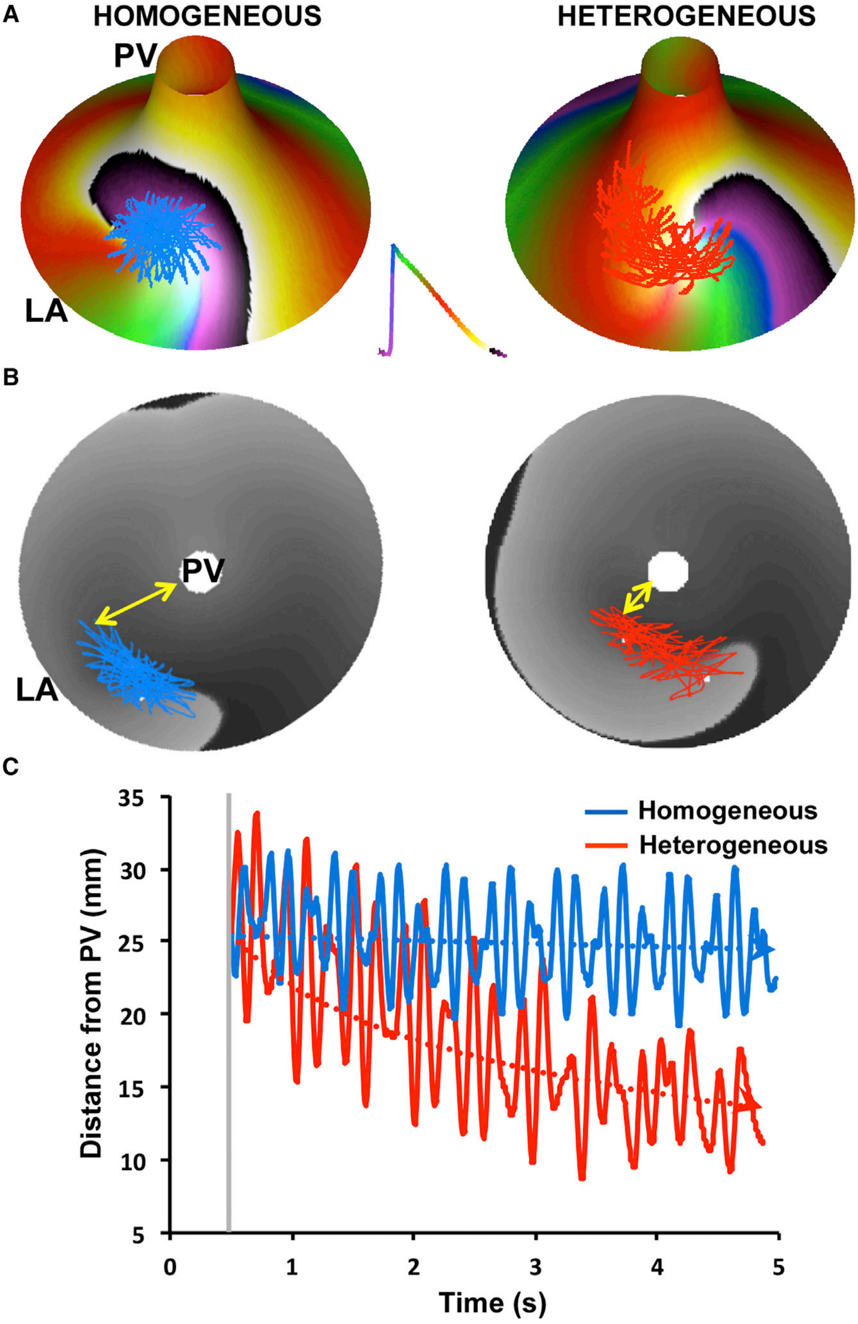

FIGURE 7 Geometry and drift. (*A*) Funnel-shaped PV-LAJ models with homogeneous (*left*) and heterogeneous (*right*, Condition I, see Fig. 1). Phase color-coded snapshot activity (see *inset*) and SP trajectory are superimposed on the model. (*B*) Bull-eye view of the models in panel *A* with voltage snapshot (*gray levels*) and SP trajectories. (*Yellow arrows*) Sample distance between the SP and the PV. (*C*) The decreasing distance between the SP and the PV edge demonstrates a PV attraction in the heterogeneous (*red*) versus the homogeneous (*blue*) model.

2. Rotor drift in the PV-LAJ can be attributed to an excitability (maximum I_{Na} availability) gradient near the rotor pivoting point.
3. In dissecting tissue properties that can explain rotor drift by conducting simple 1:1 pacing protocols, the MDP variable is a reliable predictor, independent of frequency of pacing (that is, more-positive MDP attracts rotors). And finally,
4. The generic funnel-shaped geometry and the intercellular coupling dispersion in the PV-LAJ do not alter the ionic-induced attraction of rotors toward the PV, and further suggests that the particular dispersion of transmembrane currents present in the PLA during paroxysmal AF contributes to the important role of the PVs in maintaining the arrhythmia.

Mechanisms of AF and rotor dynamics

Our understanding of AF in individual patients would benefit from knowledge of how driving rotors form and then become stable or unstable, under the conditions of multifactorial substrate heterogeneity (28,29). Paroxysmal AF in patients and in isolated normal sheep hearts has been found often to depend on fast rotors localized to the posterior wall of the LA and the PVs' region, with fibrillatory conduction toward the rest of the atria (1,2). However, the ionic properties underlying those rotors' formation and drift remain unclear (7,30). Moreover, recent studies have indicated that, in some patients, rotors that drive the AF may reside outside of the PV area (4). Our simulations demonstrate, for the first time to our knowledge, that the spatial distribution of ionic currents found in the canine PV-LAJ are conducive to attracting rotors to the PV region.

In addition, we also demonstrate that this attraction toward the LA can be reversed or arrested, if certain ionic currents are altered, which in turn may explain the variability in the location of rotors found in different patients. AF, however, may involve several coexisting rotors at any given moment. In these cases, in addition to the drift imposed by the underlying substrate, the faster rotors can also exert an overriding influence on the slower rotors (31), and the combination of these two factors on rotor dynamics warrants further investigation.

Substrate heterogeneity and rotor drift

In addition to the role of restitution characteristics of cells in rotor stability (32), simulations with gradient of excitability showed spiral-wave drifting in the direction of the region exhibiting lower excitability and velocity, with an additional perpendicular component depending on the rotor chirality (8) as well as excitability and repolarization (9), regardless of the details of the initial conditions (33). Simulations using more biophysically detailed ionic models found that for a fixed gradient in APD imposed by linearly varying potassium currents, the velocity of the drift of a rotor is a function of the magnitude of the gradient (24) and a steep gradient in APD can lead to conduction block of premature beats (34).

Our results here are in agreement with all those previous studies, but refine the previous prediction that rotors would drift toward regions with longer APD (9,23,25) to only $>80\%$ repolarization measured at frequencies close to the rotor frequency. Our simulations (Fig. 5) also show drift predictability of various measures of excitability that include ERP, $dV/dt_{\max}$, and $h\times j$ (I_{Na} availability); only MDP is able to predict drift direction, regardless of the pacing rate at which it is assessed. We also show, for the first time to our knowledge, that the attraction induced by the ionic heterogeneity is stronger than the constriction imposed by the small area in the distant PV sleeve produced by the curved geometry (Fig. 7). The homogeneous ionic condition simulation in the funnel model of the PV induces a stable, nondrifting rotor, and suggests that the smaller PV-versus-LA area increases safety for propagation toward the PV.

I_{K1}, I_{Kr}, and rotor dynamics during fibrillation

I_{K1} and I_{Kr} density gradients in the dog PV-LAJ are found to be opposing each other (16). Because recent studies have shown these two currents to be important in rotor dynamics and AF (12–14,35–37), the ionic mechanisms leading to the propensity of the PV region to favor rotor activity (17–19) became complex. We show, for the first time to our knowledge, a clear propensity of the currents distribution in the PV-LAJ to attract rotors to the PVs and the dominant role for the I_{K1} dispersion over all currents, and in particular, I_{Kr} in determining the localization of a rotor in that area. This opens the possibility that interplay between I_{K1} and I_{Kr} may be important for the differential localization of rotors in AF.

Comparing with other studies, the drift toward low I_{K1} in our study is fully consistent with the simulations by Kneller et al (21), who studied the effect of artificial heterogeneity in the inward rectifier $I_{\mathrm{K,ACh}}$ (acetylcholine-modulated inward rectifier potassium current) on AF dynamics. Although not explicitly analyzed, their simulations also suggest that while rotors accelerate their rotation frequency with increasing $I_{\mathrm{K,ACh}}$ (30), the low $I_{\mathrm{K,ACh}}$ regions are the ones that attracts rotors (21). On the other hand, a relatively recent study by Sekar et al. (38) in circular monolayers with overexpression of I_{K1} either in a central circular island, or in its periphery, showed that rotors stably pivot around the island regardless of the relative level of I_{K1}. In that study, however, the gradient was very sharp relative to the size of the rotor core, and the preparation was highly symmetrical—which may explain why that study did not show a preferential anchoring of rotors to either low or high inward rectifying K^+ current levels as observed in this and other studies (21,39).

Finally, in a recent study in cardiomyocytes monolayers with heterogeneous I_{Kr} expression, stable rotors localized to the region with the highest expression of I_{Kr} (35). Those stable rotors did not drift as in our simulations because they reside in a relatively uniform large region, in accordance with our simulations presented in Fig. S5.

Limitations

We study a specific set of membrane kinetic models (CRN-K) with a Boltzmann distribution of the current densities across the PV-LAJ; kinetic models preferred because of extensive validation of propagation properties (22,40) over a more recent and detailed model requiring adjustments (41,42). Experimental or clinical data on ionic properties and dispersion in the atria are scarce; we focused on the effect of reported ionic currents data for the dog. However, attraction or repulsion of rotors by the PVs at the PVLAJ may be affected by factors other than those studied here. For example, the heterogeneity in the intrinsic cellular properties may have different effective heterogeneity in refractoriness and excitability (33) depending on structural intercellular coupling (43), fibrosis (44), or the size of the medium (34,45–47). Further, the drift of rotors may be further influenced by accumulations or intra- or extracellular ions, as has been shown to occur in AF (48).

In our study, we ruled-out that PV funnel-like anatomy reverses the ionic-induced attraction to the PVs. However, additional anatomical factors such as wall thickness (49,50), the fiber bundles (51), or fibrosis (7) may also regulate the drift of rotors, possibly even counteracting the drift trend caused by the ionic gradients. To mitigate these limitations, we focused in our study on conditions relevant only to paroxysmal AF before any remodeling and fibrosis, and incorporated various possible I/V relationships to substantiate our conclusions regarding the I_{K1} dominance and drift prediction (Fig. 6 and also Fig. S6, Fig. S7, and Fig. S8). Our study nevertheless should be considered only as a first step in elucidating the concept of heterogeneity-induced drift, and needs to be tested in future experimental studies.

CONCLUSIONS

Consistent with experimental and clinical studies on paroxysmal AF, simulations in an ionically heterogeneous model of the PV-LAJ showed rotor attraction toward the PVs, consistent with reduced coupling and despite spatial constriction in the PV region. Our simulations suggest that I_{K1} heterogeneity across the PV-LAJ is dominant compared to other currents in conveying drift direction through its effect on refractoriness and excitability. Our simulations also suggest that measuring with high-resolution refractoriness, excitability, and diastolic potentials during pacing could provide a mechanistic guidance for the unstable components of rotors that are believed to underlie AF.

SUPPORTING MATERIAL

Detailed Methods and Supplementary Discussion, with one movie, eight figures, and references (52–55) are available at http://www.biophysj.org/biophysj/supplemental/S0006-3495(14)00273-2.

We thank Dr. Sandeep Pandit for discussions and help in preparing the manuscript.

Supported in part by National Heart, Lung, and Blood Institute grants (Nos. P01-HL039707, P01-HL08722, and R01-HL118304); the Coulter Foundation from the Biomedical Engineering Department (University of Michigan); the Gelman Award from the Cardiovascular Division (University of Michigan); and the Leducq Foundation. Also supported in part by Faro Global MICINN-FGUVa grant No. FG/US/0775/2009, PROMETEO grant No. 2010-093, and a BEST/2011 grant from Generalitat Valenciana and the Cardiovascular Protection Excellence Research microcluster, VLC-Campus (Spain).

REFERENCES

1. Mandapati, R., A. Skanes, …, J. Jalife. 2000. Stable microreentrant sources as a mechanism of atrial fibrillation in the isolated sheep heart. *Circulation.* 101:194–199.
2. Atienza, F., J. Almendral, …, O. Berenfeld. 2006. Activation of inward rectifier potassium channels accelerates atrial fibrillation in humans: evidence for a reentrant mechanism. *Circulation.* 114:2434–2442.
3. Cuculich, P. S., Y. Wang, …, Y. Rudy. 2010. Noninvasive characterization of epicardial activation in humans with diverse atrial fibrillation patterns. *Circulation.* 122:1364–1372.
4. Narayan, S. M., D. E. Krummen, …, J. M. Miller. 2012. Treatment of atrial fibrillation by the ablation of localized sources: CONFIRM (conventional ablation for atrial fibrillation with or without focal impulse and rotor modulation) trial. *J. Am. Coll. Cardiol.* 60:628–636.
5. Cherry, E. M., J. R. Ehrlich, …, F. H. Fenton. 2007. Pulmonary vein reentry—properties and size matter: insights from a computational analysis. *Heart Rhythm.* 4:1553–1562.
6. Sanders, P., O. Berenfeld, …, M. Haïssaguerre. 2005. Spectral analysis identifies sites of high-frequency activity maintaining atrial fibrillation in humans. *Circulation.* 112:789–797.
7. Tanaka, K., S. Zlochiver, …, J. Kalifa. 2007. Spatial distribution of fibrosis governs fibrillation wave dynamics in the posterior left atrium during heart failure. *Circ. Res.* 101:839–847.
8. Pertsov, A. M., J. M. Davidenko, …, J. Jalife. 1993. Spiral waves of excitation underlie reentrant activity in isolated cardiac muscle. *Circ. Res.* 72:631–650.
9. Fast, V. G., and A. M. Pertsov. 1990. Drift of vortex in the myocardium [Dreĭf vikhria v miokarde]. *Biofizika.* 35:478–482.
10. Nattel, S., B. Burstein, and D. Dobrev. 2008. Atrial remodeling and atrial fibrillation: mechanisms and implications. *Circ. Arrhythm. Electrophysiol.* 1:62–73.
11. Schram, G., M. Pourrier, …, S. Nattel. 2002. Differential distribution of cardiac ion channel expression as a basis for regional specialization in electrical function. Review. *Circ. Res.* 90:939–950.
12. Hou, L., M. Deo, …, J. Jalife. 2010. A major role for HERG in determining frequency of reentry in neonatal rat ventricular myocyte monolayer. *Circ. Res.* 107:1503–1511.
13. Noujaim, S. F., S. V. Pandit, …, J. Jalife. 2007. Up-regulation of the inward rectifier K^+ current (I_{K1}) in the mouse heart accelerates and stabilizes rotors. *J. Physiol.* 578:315–326.
14. Pandit, S. V., and J. Jalife. 2013. Rotors and the dynamics of cardiac fibrillation. Review. *Circ. Res.* 112:831–833.
15. Ehrlich, J. R., T. J. Cha, …, S. Nattel. 2003. Cellular electrophysiology of canine pulmonary vein cardiomyocytes: action potential and ionic current properties. *J. Physiol.* 551:801–813.
16. Cha, T. J., J. R. Ehrlich, …, S. Nattel. 2005. Atrial tachycardia remodeling of pulmonary vein cardiomyocytes: comparison with left atrium and potential relation to arrhythmogenesis. *Circulation.* 111:728–735.
17. Lemola, K., D. Chartier, …, S. Nattel. 2008. Pulmonary vein region ablation in experimental vagal atrial fibrillation: role of pulmonary veins versus autonomic ganglia. *Circulation.* 117:470–477.
18. Po, S. S., Y. Li, …, E. Patterson. 2005. Rapid and stable re-entry within the pulmonary vein as a mechanism initiating paroxysmal atrial fibrillation. *J. Am. Coll. Cardiol.* 45:1871–1877.
19. Arora, R., S. Verheule, …, J. E. Olgin. 2003. Arrhythmogenic substrate of the pulmonary veins assessed by high-resolution optical mapping. *Circulation.* 107:1816–1821.
20. Courtemanche, M., R. J. Ramirez, and S. Nattel. 1998. Ionic mechanisms underlying human atrial action potential properties: insights from a mathematical model. *Am. J. Physiol.* 275:H301–H321.
21. Kneller, J., R. Zou, …, S. Nattel. 2002. Cholinergic atrial fibrillation in a computer model of a two-dimensional sheet of canine atrial cells with realistic ionic properties. *Circ. Res.* 90:E73–E87.
22. Pandit, S. V., O. Berenfeld, …, J. Jalife. 2005. Ionic determinants of functional reentry in a 2-D model of human atrial cells during simulated chronic atrial fibrillation. *Biophys. J.* 88:3806–3821.
23. Davidenko, J. M., A. V. Pertsov, …, J. Jalife. 1992. Stationary and drifting spiral waves of excitation in isolated cardiac muscle. *Nature.* 355:349–351.
24. Ten Tusscher, K. H., and A. V. Panfilov. 2003. Reentry in heterogeneous cardiac tissue described by the Luo-Rudy ventricular action potential model. *Am. J. Physiol. Heart Circ. Physiol.* 284:H542–H548.

25. Dhamoon, A. S., S. V. Pandit, …, J. M. Anumonwo. 2004. Unique Kir_2.X properties determine regional and species differences in the cardiac inward rectifier K^+ current. *Circ. Res.* 94:1332–1339.

26. Chaldoupi, S. M., P. Loh, …, H. V. van Rijen. 2009. The role of connexin40 in atrial fibrillation. *Cardiovasc. Res.* 84:15–23.

27. Berenfeld, O., and A. M. Pertsov. 1999. Dynamics of intramural scroll waves in three-dimensional continuous myocardium with rotational anisotropy. *J. Theor. Biol.* 199:383–394.

28. Jalife, J. 2003. Experimental and clinical AF mechanisms: bridging the divide. *J. Interv. Card. Electrophysiol.* 9:85–92.

29. Oral, H. 2005. Mechanisms of atrial fibrillation: lessons from studies in patients. *Prog. Cardiovasc. Dis.* 48:29–40.

30. Sarmast, F., A. Kolli, …, J. Jalife. 2003. Cholinergic atrial fibrillation: $I_{K,ACh}$ gradients determine unequal left/right atrial frequencies and rotor dynamics. *Cardiovasc. Res.* 59:863–873.

31. Davidenko, J. M., R. Salomonsz, …, J. Jalife. 1995. Effects of pacing on stationary reentrant activity. Theoretical and experimental study. *Circ. Res.* 77:1166–1179.

32. Kléber, A. G., and Y. Rudy. 2004. Basic mechanisms of cardiac impulse propagation and associated arrhythmias. *Physiol. Rev.* 84: 431–488.

33. Wellner, M., A. M. Pertsov, and J. Jalife. 1999. Spiral drift and core properties. *Phys. Rev. E Stat. Phys. Plasmas Fluids Relat. Interdiscip. Topics.* 59 (5 Pt A):5192–5204.

34. Sampson, K. J., and C. S. Henriquez. 2001. Simulation and prediction of functional block in the presence of structural and ionic heterogeneity. *Am. J. Physiol. Heart Circ. Physiol.* 281:H2597–H2603.

35. Campbell, K., C. J. Calvo, …, J. Jalife. 2012. Spatial gradients in action potential duration created by regional magnetofection of hERG are a substrate for wavebreak and turbulent propagation in cardiomyocyte monolayers. *J. Physiol.* 590:6363–6379.

36. Noujaim, S. F., J. A. Stuckey, …, J. Jalife. 2010. Specific residues of the cytoplasmic domains of cardiac inward rectifier potassium channels are effective antifibrillatory targets. *FASEB J.* 24:4302–4312.

37. Amit, G., K. Kikuchi, …, J. K. Donahue. 2010. Selective molecular potassium channel blockade prevents atrial fibrillation. *Circulation.* 121:2263–2270.

38. Sekar, R. B., E. Kizana, …, L. Tung. 2009. I_{K1} heterogeneity affects genesis and stability of spiral waves in cardiac myocyte monolayers. *Circ. Res.* 104:355–364.

39. Samie, F. H., O. Berenfeld, …, J. Jalife. 2001. Rectification of the background potassium current: a determinant of rotor dynamics in ventricular fibrillation. *Circ. Res.* 89:1216–1223.

40. Zlochiver, S., M. Yamazaki, …, O. Berenfeld. 2008. Rotor meandering contributes to irregularity in electrograms during atrial fibrillation. *Heart Rhythm.* 5:846–854.

41. Grandi, E., S. V. Pandit, …, D. M. Bers. 2011. Human atrial action potential and Ca^{2+} model: sinus rhythm and chronic atrial fibrillation. *Circ. Res.* 109:1055–1066.

42. Deo, M., Y. Ruan, …, S. G. Priori. 2013. KCNJ2 mutation in short QT syndrome-3 results in atrial fibrillation and ventricular proarrhythmia. *Proc. Natl. Acad. Sci. USA.* 110:4291–4296.

43. Bub, G., A. Shrier, and L. Glass. 2005. Global organization of dynamics in oscillatory heterogeneous excitable media. *Phys. Rev. Lett.* 94:028105.

44. Ashihara, T., R. Haraguchi, …, N. A. Trayanova. 2012. The role of fibroblasts in complex fractionated electrograms during persistent/permanent atrial fibrillation: implications for electrogram-based catheter ablation. *Circ. Res.* 110:275–284.

45. Viswanathan, P. C., R. M. Shaw, and Y. Rudy. 1999. Effects of I_{Kr} and I_{Ks} heterogeneity on action potential duration and its rate dependence: a simulation study. *Circulation.* 99:2466–2474.

46. Sampson, K. J., and C. S. Henriquez. 2002. Interplay of ionic and structural heterogeneity on functional action potential duration gradients: implications for arrhythmogenesis. *Chaos.* 12:819–828.

47. Sampson, K. J., and C. S. Henriquez. 2005. Electrotonic influences on action potential duration dispersion in small hearts: a simulation study. *Am. J. Physiol. Heart Circ. Physiol.* 289:H350–H360.

48. Miyata, A., J. D. Dowell, …, M. Rubart. 2002. Rate-dependent $[K^+]_o$ accumulation in canine right atria in vivo: electrophysiological consequences. *Am. J. Physiol. Heart Circ. Physiol.* 283:H506–H517.

49. Zhao, J., T. D. Butters, …, B. H. Smaill. 2012. An image-based model of atrial muscular architecture: effects of structural anisotropy on electrical activation. *Circ Arrhythm Electrophysiol.* 5:361–370.

50. Yamazaki, M., S. Mironov, …, J. Kalifa. 2012. Heterogeneous atrial wall thickness and stretch promote scroll waves anchoring during atrial fibrillation. *Cardiovasc. Res.* 94:48–57.

51. Klos, M., D. Calvo, …, J. Kalifa. 2008. Atrial septopulmonary bundle of the posterior left atrium provides a substrate for atrial fibrillation initiation in a model of vagally mediated pulmonary vein tachycardia of the structurally normal heart. *Circ Arrhythm Electrophysiol.* 1:175–183.

52. Woźniak-Skowerska, I., M. Skowerski, …, M. Trusz-Gluza. 2011. Comparison of pulmonary veins anatomy in patients with and without atrial fibrillation: analysis by multislice tomography. *Int. J. Cardiol.* 146:181–185.

53. Verheule, S., E. E. Wilson, …, J. E. Olgin. 2002. Tissue structure and connexin expression of canine pulmonary veins. *Cardiovasc. Res.* 55:727–738.

54. Zlochiver, S., V. Muñoz, …, J. Jalife. 2008. Electrotonic myofibroblast-to-myocyte coupling increases propensity to reentrant arrhythmias in two-dimensional cardiac monolayers. *Biophys. J.* 95: 4469–4480.

55. Warren, M., P. K. Guha, …, J. Jalife. 2003. Blockade of the inward rectifying potassium current terminates ventricular fibrillation in the guinea pig heart. *J. Cardiovasc. Electrophysiol.* 14:621–631.

Attraction of Rotors to the Pulmonary Veins in Paroxysmal Atrial Fibrillation: A Modeling Study

Conrado J Calvo, Makarand Deo, Sharon Zlochiver, José Millet, Omer Berenfeld

SUPPLEMENTAL MATERIAL

CONTENT

NON-STANDARD ABBREVIATIONS AND ACRONYMS

AP: Action potential
APD: Action potential duration
AF: Atrial fibrillation
Condition I: All currents varied spatially in the model.
Condition II: All currents, except I_{K1}, varied spatially in the model
Condition III: Only I_{K1} varied spatially in the model
CRN-K: Courtemanche-Ramirez-Nattel and Kneller model of the human atrial cell kinetics
CV: Conduction velocity
DF: Dominant frequency
dV/dt_{max}: Maximum upstroke velocity
ERP: Effective refractory period
G_x: Maximum conductance of channel x
h×j: The fraction of sodium channels available for activation
$h \times j_{peak}$: The maximum fraction of sodium channels available for activation during a cycle
I_{K1}: Inward rectifier potassium current
$I_{K,ACh}$: Acetylcholine modulated inward rectifier potassium current
I_{Kr}: Rapid delayed rectifier potassium current
I_{Ks}: Slow delayed rectifier potassium current
I_{to}: Outward transient potassium current
I_{Na}: Sodium current
I_{CaL}: L-type calcium current
I-V: Relationship between the current density and transmembrane voltage
LA: Left atrium
LV: Left ventricle
MDP: Minimum diastolic transmembrane potential
PVs: Pulmonary veins
PV-LAJ: LA and PV junction
RV: Right ventricle
SP: Singularity point. Used to indicate the pivoting location of a rotor
S1, S2: Two sequential stimulations at particular times and locations
TSP: Time-space plot

DETAILED METHODS

Structural Models

Numerical simulations were performed on 2- and pseudo 3-dimensional structures of the area of transition between the LA and the PV (see Fig. 1) with increasing anatomical realism as:

1. A 50×50 mm^2 regular 2D square model was implemented by no-flux boundary conditions.
2. A pseudo-3D cylindrical surface model constructed by applying no-flux boundary conditions at the LA and PV edges and periodic boundary conditions on the other two edges of a regular 2D mesh.
3. A pseudo-3D funnel-shaped surface was constructed with near-equilateral triangulated mesh with no-flux conditions on the wide (LA) and narrow (PV) edges. The height of the funnel model was set to 30 mm and its diameter was set to increase exponentially from 10 mm at the PV to 48 mm at the LA edges (see Fig. 1) (1). Our LA-PVJ funnel model represents a typical right superior PV as described by (1). The radii of the PV and LA where selected such that the radius at the ostia location (15 mm from the LA-end) is where the 50% Boltzmann factor was placed. The funnel-like geometry model was generated by circumscribing an exponent function around the central axis of the LA-PVJ. Accordingly we created the shape of the funnel with the radius r as a function of the distance from the PV edge as: $r = R + A*\exp(z/B)$, (R, A and B are distance constants) where z, the distance along that axis, was increased with a non-uniform steps that maintained the distance between the rings on the surface of the funnel ($\Delta z^2 + \Delta r^2$) approximately constant. Following, the 3D set of nodes was meshed using the Delaunay triangulation scheme resulting in a quasi-equilateral triangular connectivity with an average intermodal distance of 0.1 mm and standard deviation of less than 0.01 mm.

Ionic Modeling

The transmembrane potential at each node was based on the Courtemanche-Ramirez-Nattel and Kneller (CRN-K) model of human atrial cell kinetics in the presence of acetylcholine (ACh) (2-4). I_{KACh} kinetics was based on the formulation by Kneller et al (3) with a minimal amount of [ACh]=0.0015 µM to enable rotors in the CRN model of the atria (4):

$$I_{K,ACh} = \left(\frac{10}{1+\frac{9.12652}{[ACh]^{0.477811}}}\right)\cdot\left(0.013384+\frac{0.22663}{1+\exp\left(\frac{V+80.253}{50.714}\right)}\right)\cdot(V-E_K) \qquad \text{(Eq. 1)}$$

where V (mV) is the transmembrane potential and E_K (mV) is the potassium reversal potential. Compatibility of action potentials calculated at 1 Hz pacing between this study and those by Kneller et al (3) was confirmed. In the simulations presented in Fig. S6, the formulation for I_{K1} based on the Kir2.1 or Kir2.3 isoforms was as reported by Dhamoon et al (5) and differing from the CRN-K model (2-3):

$$I_{K1} = a_4 + \frac{a_1\cdot(V-E_K)}{a_2+\exp[a_3\cdot(V-E_K)]}\,. \qquad \text{(Eq. 2)}$$

Table ST1 contains values of the a_1-a_4 parameters in Eq. 2 fitted for I_{K1} consisting of either Kir2.1 or Kir2.3 isoforms (5):

Table ST1. Coefficients for data fitted for Kir2.1 and Kir2.3 in the I_{K1} of Eq. 2. (5)

Current (isoform)	**Coefficient**	**Value**
I_{K1} (Kir2.1)	a_1	0.4719
	a_2	7.1202
	a_3	0.1187
	a_4	0.0
I_{K1} (Kir2.3)	a_1	0.048
	a_2	0.0333
	a_3	0.2227
	a_4	-0.0607

Simulations and Conditions

Electrical activity was coded in C and MPI and computed on the Flux High Performance Computing cluster at the University of Michigan using a mono-domain, finite volume discretization (FVM), Euler forward scheme with 100 µm internodal distance (h), 0.005 ms time step (Δt), and isotropic diffusion coefficient of 0.062 mm^2/ms (D) adjusted for conduction velocity (CV) of 48 cm/s. Numerical stability of the solutions was assured. During propagation neither irregular (squared, mesh affected) wavefront curvature nor instability of the action potentials, nor any numerical artifacts were observed. Additionally, we verified that our simulations parameters satisfy the 2-dimensional Nyquist stability criterion (6): $D\cdot\Delta t/h^2 < 1/(2\cdot\text{dimensions})$ which yields $0.031 < 0.25$. Initial conditions were the steady state membrane variables following pacing a single cell at 1 Hz for 10 s.

Heterogeneous ionic conditions were implemented by assigning a spatial Boltzmann ($x_{1/2}$ = 25 mm and Δx = 5 mm) distribution of conductance for I_{K1}, I_{Ks}, I_{Kr}, I_{to}, and I_{CaL} between the LA and the PV based on data from dogs (7) and described in Fig. 1A (maximal conductance for I_{Kr} and I_{ks} where increased by 50% and 60% respectively while I_{K1}, I_{to} and I_{CaL} where diminished by 42%, 25% and 30% respectively). Three conditions of heterogeneity were modeled: 1) all currents varied spatially according their corresponding Boltzmann function (Condition I); 2) all currents, except I_{K1}, varied (Condition II); 3) only I_{K1} varied in space (Condition III).

To investigate the effect of the heterogeneous intercellular coupling in the LA-PV junction (8) on rotor drift in combination with the ionic heterogeneities additional 50×50 mm^2 models were generated with gradients in the isotropic intercellular coupling coefficient. The intercellular coupling in those models was set to vary following a Boltzmann profile (Fig. 1) between a baseline level at the LA edge of the model (as set in all other conditions) to a 25% smaller value at the PV edge (9).

Rotors Initiation and Characterization

Rotors were initiated by cross-field stimulations and the instantaneous center of rotation was tracked by its phase singularity point (SP) in the Hilbert-transformed movies (10,11) (see Fig. S1). In the cylindrical model, two counter-rotating (opposite chirality) rotors were generated and shown to follow a similar drift dynamics. The SP of a rotor was defined as the instantaneous location toward which all the phases in space converged and automatically detected and tracked based on the point-by-point (resolution of about 1 mm) circumferential sum of neighboring phases exhibiting a monotonic progression to approximately 2π (See movie SM1 illustrating continuous detection of SP.) For controls, rotors were initiated in two separated 2D models with either homogeneous LA or PV ionic conductances (in the absence of spatial heterogeneities) and characterized by their rotation frequency, the I_{Na} gating parameters h×j (I_{Na} availability), core size as well as wavefront curvature, action potential duration (APD), wavefront conduction velocity (CV) magnitude and wavelength (WL) of excitation (12,14) determined at 70%

amplitude (Fig. S2). Those parameters are presented for the two simulations as a function of the distance from the SP (Fig. S2, panel B). The wave front and tail were identified as a continuous isopotential line. During reentry, activation maps were generated at 50% amplitude and used to obtain local CV vector maps. The WL was calculated as the distance between the tail and the front of a wave along the CV vectors (Fig. S2, Panel B).

Data Analysis

To obtain a measure of effective refractory period (ERP) at a specific stimulation cycle length (CL) we first simulated activity for 10 s to generate steady state conditions at individual cell level and then determined the stimulus strength in the tissue model at ×1.5 the minimum excitation threshold current for a 1 mm virtual pacing electrode. Measurement consisted in 10 S1 stimuli train at CL of 1000, 500 or 140 ms, followed by an S2 premature stimulus at decreasing interval. ERP value was defined as the last (shortest) S2 allowing excitation. Measurements were repeated at 6 locations across the models.

Methods used for the parameter measurements from the numerical simulations have been previously described (13,14). Spatial profiles (between the LA and the PV edges) of APD and peak sodium availability $(h\times j)_{peak}$ were obtained by averaging those parameters in time for every pixel across the model in the last 2 s of the respective 5 s simulation. Measurements of minimal diastolic potential (MDP) and maximal upstroke velocity $(dV/dt)_{max}$ followed same temporal procedure.

SUPPLEMENTARY DISCUSSION

Ventricular fibrillation in guinea-pigs isolated hearts is driven by stable rotors in the left ventricle (LV) where the outward component of I_{K1} was found to be higher than the right ventricle (RV) (15,16). At first, the predictions in the present study suggesting that rotors would stabilize at the lowest I_{K1} region seem to conflict with those previous findings, but a deeper examination reveals that the two studies are complimentary; The present study considers rotors with a core dimension of about 11 mm (Fig. S2) that extends over an area that is wider than the distance of about 5 mm in which a gradient of currents was measured in the canine posterior LA (Fig. 1) (17,18). Moreover, our simulations here focus on currents heterogeneities that are continuous and monotonic, and in the absence of any structural heterogeneity. In the guinea-pigs study on the other hand, we have no data on the transition in the density of currents other than I_{K1}, between the LV and RV, which may be present uniformity over areas larger than the core size, thus enabling the rotor's stabilization in the larger I_{K1} zone (Fig. S5). Moreover, various anatomical components, such as the papillary bundle, are likely to present additional anchoring factors further stabilizing a driving rotor.

MOVIE SM1 DESCRIPTION

A video clip illustrating the drift of counter-rotating rotors in the heterogeneous PV-LA junction toward the PV edge of the model (Condition I, see also Fig. S1). The bottom plane is a gray-scale movie of the voltage; the upper plane is the phase movie of the voltage movie. The phase movie is used for detection of the 2 SP which are projected on the voltage map below and whose time trajectory is superimposed on the voltage movie (yellow traces) and also upward in the time axis.

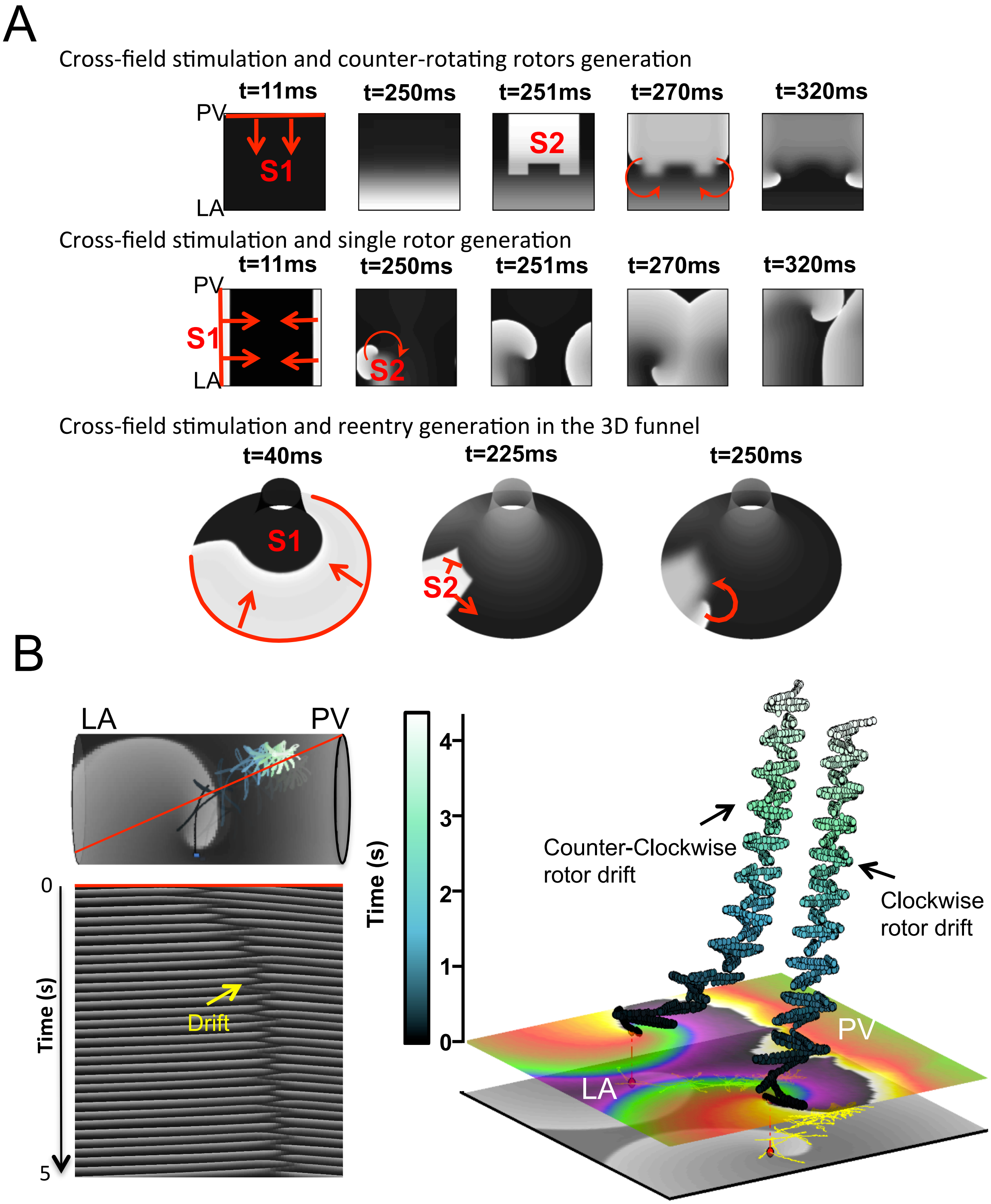

Fig. S1: Rotors initiation and tracking. A. Cross-field stimulation leading to two counter rotating or a single rotor in the cylindrical, flat and funnel-like models. Gray-scale corresponds to voltage (black, resting; white excited). Red lines: Location of S1. B. Left: Demonstration of the automatic SP tracking of a drifting rotor as the TSP (bottom) matches the SP trajectory superimposed on the cylinder model (Condition I, top). Right: In a flat model (Condition I), coexisting clockwise and counter-clockwise rotors drift toward the PV, as illustrated by the 3D TSP trajectories whose origin is at the SP in the phase map at t=0 (see movie SM1).

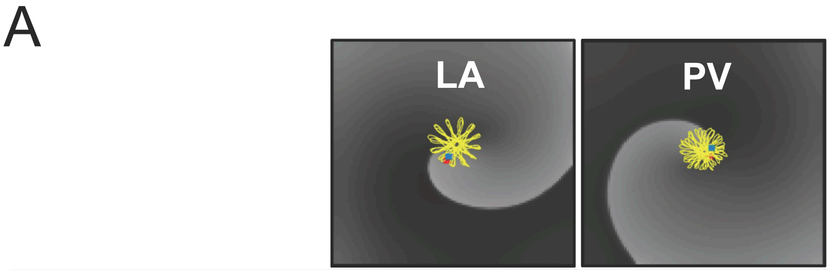

Core diameter (mm)	11.5	11.3
Rotor frequency (Hz)	7.7	7
Space and time <h×j>	0.38	0.29

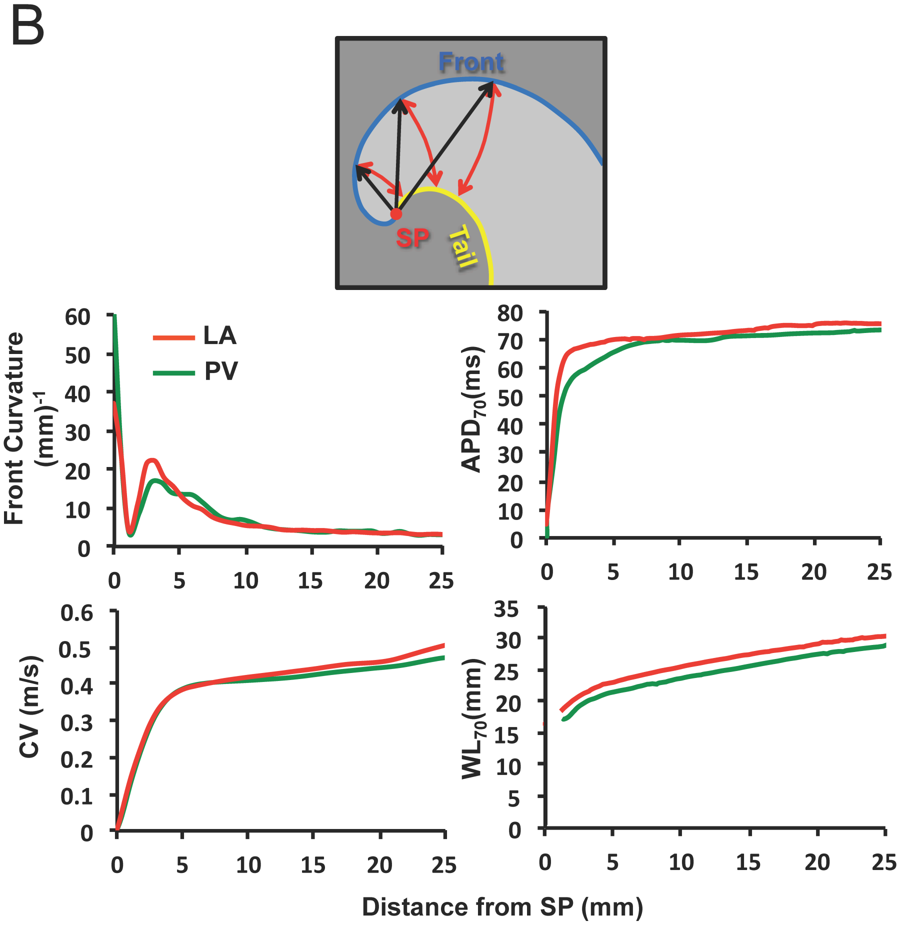

Fig. S2: Rotors characterization in homogeneous LA and PV models. The baseline relationship between the substrate and single rotor was studied in separated 2D models with homogeneous ionic conductances of the LA and PV. A. Tracking SP reveals a meandering (yellow traces), without drift, in an area of diameters of about 11.4 mm. The LA rotor was slightly faster at 7.7 Hz in comparison with PV rotor at 7 Hz, which was consistent with larger space-time averaged sodium channels availability, h·j, in the LA (0.38) than in the PV (0.29). (4) B. Top diagram illustrates the WL (red) as the distance between the isopotentials of front (blue) and tail (yellow) along the CV vectors (not shown) and distance to SP (black). Bottom graphs show rotor properties that qualitatively similar in the LA and PV, but can reach point-wise differences of up to about 20-30%.

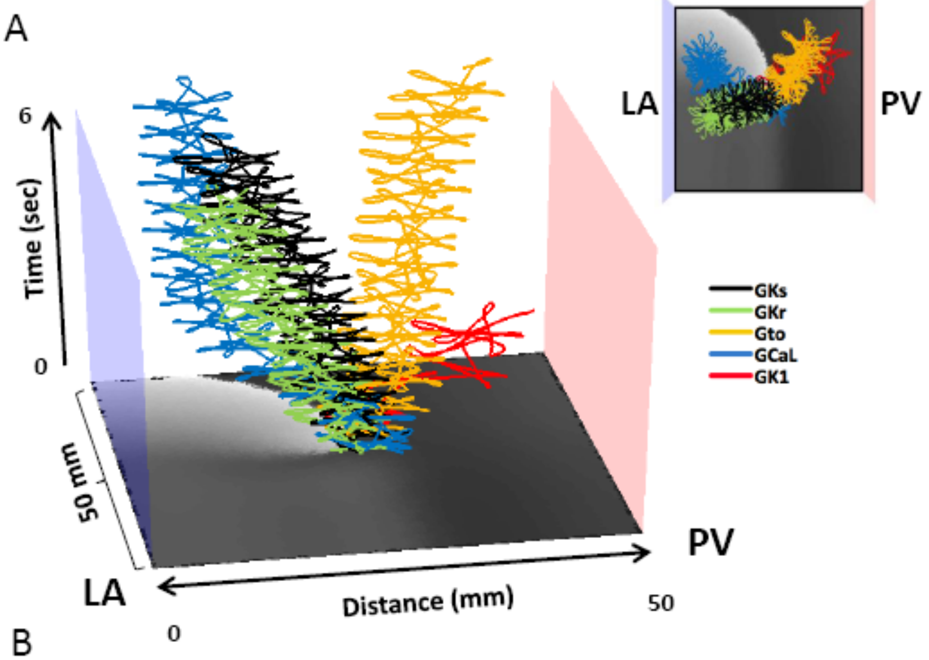

B

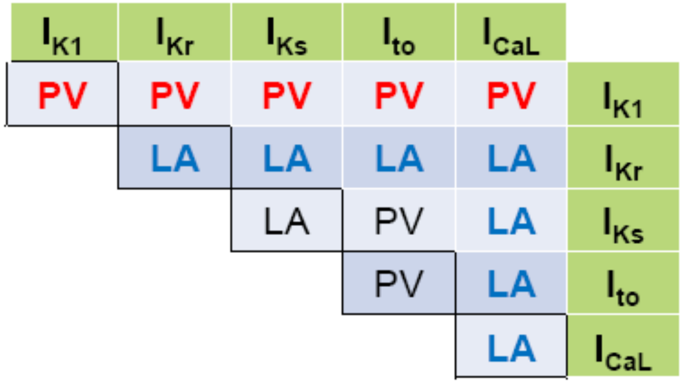

	I_{K1}	I_{Kr}	I_{Ks}	I_{to}	I_{CaL}
I_{K1}	PV	PV	PV	PV	PV
I_{Kr}		LA	LA	LA	LA
I_{Ks}			LA	PV	LA
I_{to}				PV	LA
I_{CaL}					LA

Fig. S3. Spatial gradients of individual and paired currents and reentry drift. A. Effect of spatial gradient for each individual current on rotor drift. 2D PV-LAJ model showing spatio-temporal trajectories of SPs of rotors in gradients of I_{Ks} (black), I_{kr} (green), I_{to} (yellow), I_{CaL} (blue) and I_{K1} (red) as described by the individual Boltzmann distributions in Panel A of Fig. 1. While I_{to} and I_{K1} cause the rotor to drift toward the PV edge, the gradients in the other currents cause the rotor to drift toward the opposite LA edge. Insert: top view of the trajectories. B. Effect of spatial gradients in paired currents on rotor drift. The table shows the direction of the drift when ionic gradients as indicated in the abscissa and ordinate (green cells) were considered. I_{K1} is the only current whose gradient leads to PV attraction (in red fonts) of the rotor regardless of gradient in any other current.

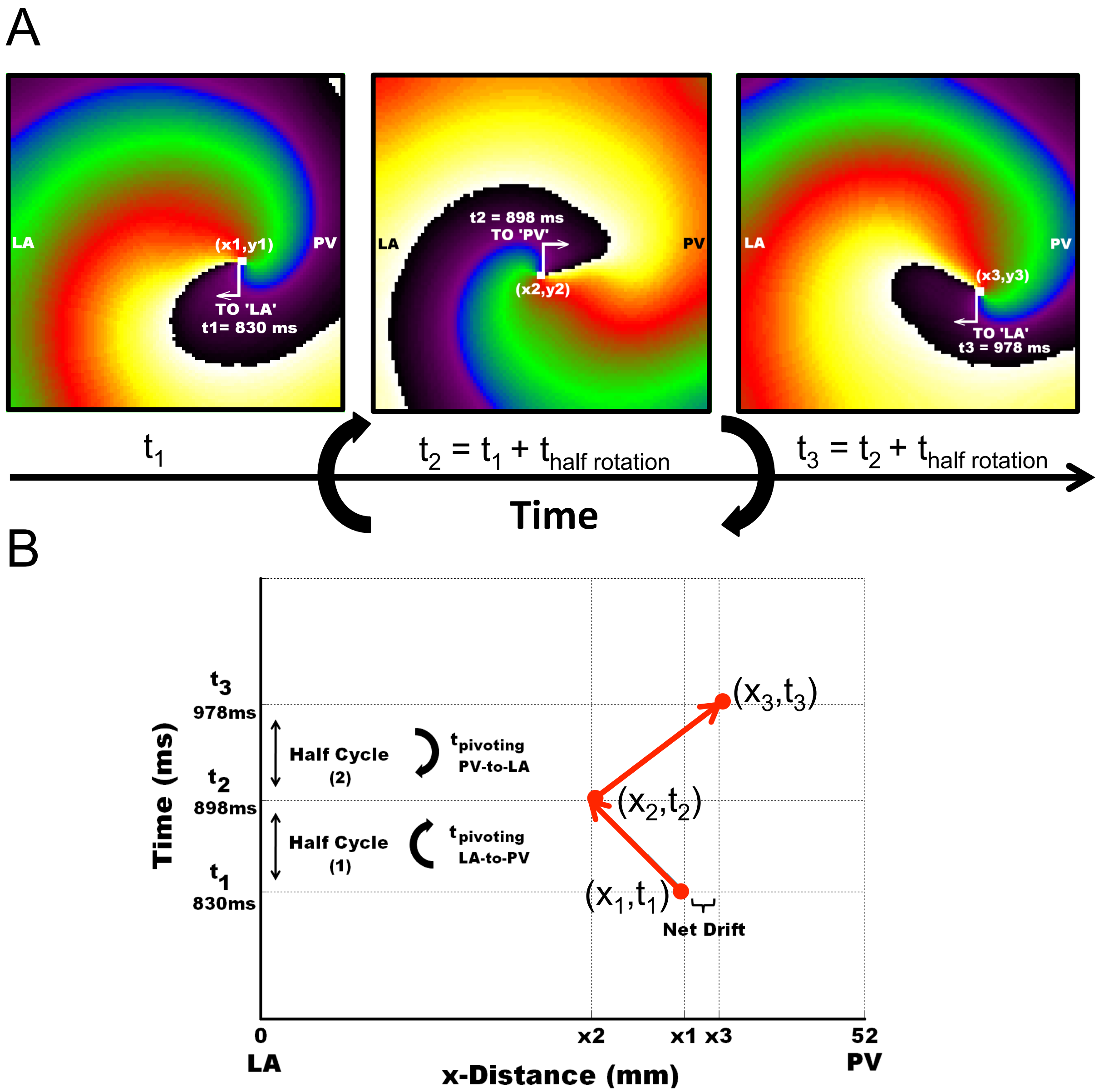

Fig. S4. Linking rotor pivoting to rotor drift. The process whereby the region with reduced excitability (h·j) attracts a rotor. A. Snapshots of the rotor at 3 moments: t_1 = 830 ms is a random reference time in which the front near the SP points toward the LA; t_2 = 898 ms is a time half a rotation later in which the front near the SP points toward the PV; t_3 = 978 ms is a time half a rotation later in which the front near the SP points again toward the LA and the rotor has completed a full rotation after t_1. The locations of the SP of the rotor at these 3 times are designated (x_1,y_1), (x_2,y_2) and (x_3,y_3), respectively. B. A time-space plot describing the trajectory of the rotor along the x direction (red arrows). The time it takes the rotor to complete its first half rotation is $t_2–t_1$=68 ms is shorter than the time it takes to rotor to complete its second half rotation $t_3–t_2$=78 ms. During that prolonged time the drift toward the PV, ($x_3 – x_2$), is larger than the drift toward the LA, ($x_2 – x_1$), resulting in a net drift, ($x_3 – x_1$), toward the PV once the full rotation is completed.

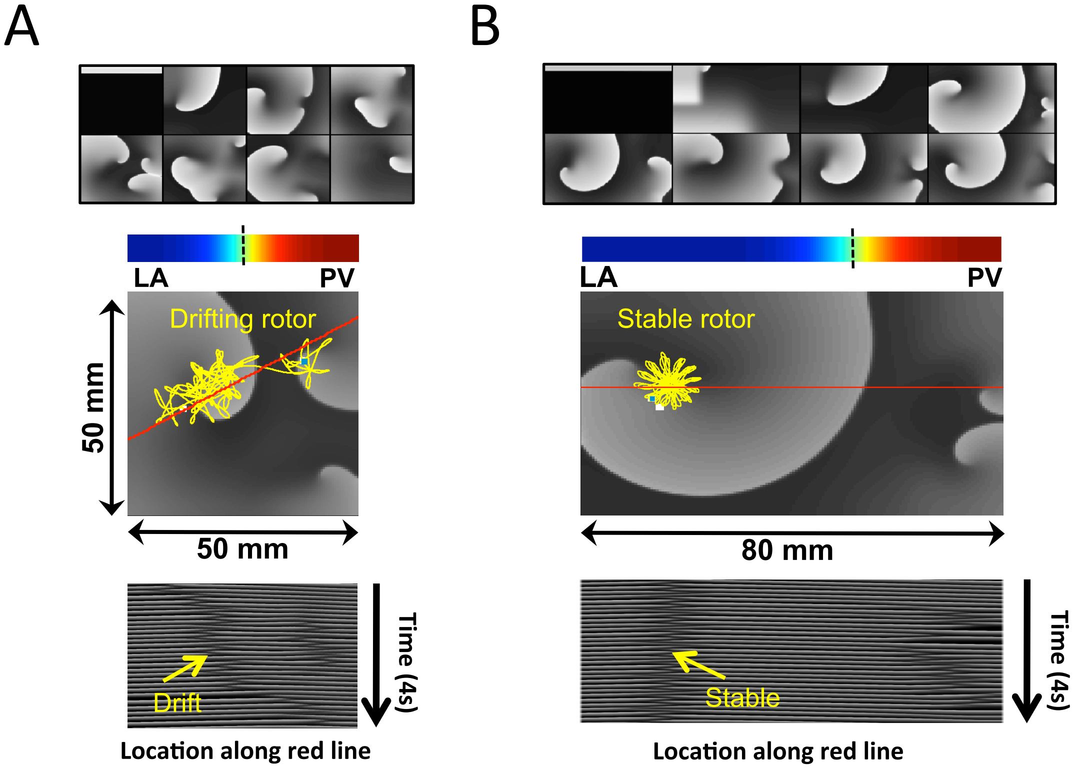

Fig. S5. Ionic gradient at the core region and rotor drifting. Here we demonstrate that heterogeneity is required within the core region to induce rotor drift. A. Simulation in a 50×50 mm^2 model of the PV-LAJ whose Boltzmann distribution is varying throughout the model (Condition I). B. Simulation in a 80×50 mm^2 model of the PV-LAJ whose Boltzmann distribution is mostly uniform in the LA portion of the model. Top panels: Sequential voltage snap shots (left to right and top to bottom) of the spontaneous time-course of a rotor initiated in the LA portion of the model. Color bars: The normalized Boltzmann factor variation from the LA (blue, 0) to the PV (red, 1) edges (see Fig. 1). The dash vertical line illustrates the steepest gradient location. It is appreciated that there is a large area in the LA portion of the model in B that is uniformly zero (blue). The time-space plots (bottom) taken along the red lines of the models show that the core size (vertical dark gray band) is smaller than the area with LA uniform conditions in B, but not so in A, enabling a stable rotor in LA region, without a drift, in B but not in A. The appearance of a stable LA rotor in B is consistent with the stable rotor demonstrated recently by Campbell et al in a 35-mm wide monolayer of cardiomyocytes with a relatively more step-wise heterogeneity in I_{Kr} expression (Boltzmann Δx of about 1 mm compared to 5 mm in the present study) (12).

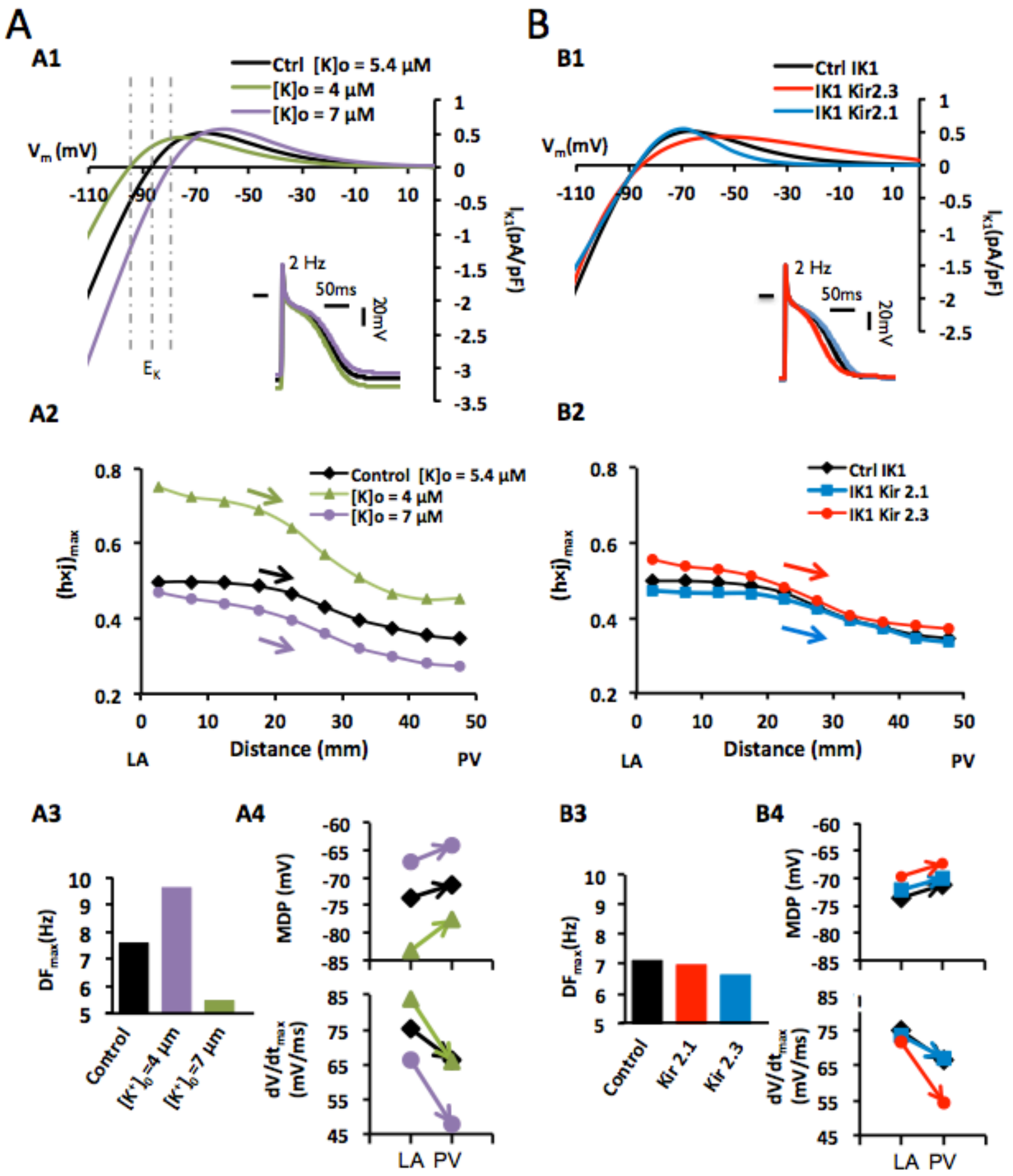

Fig. S6. Effect of $[K]_o$ and major I_{K1} isoforms on rotor drift direction. A. Investigating the effect of $[K]_o$ on rotor drift. A1. I_{K1} I-V curves under conditions of normal, reduced and increased $[K]_o$ demonstrate shifting of the reversal potential and altering slope resistance as well as outward current properties. A2. Rotors drifted toward the excitability sink (lowest h×j) at the PVs for all $[K]_o$ levels. A3. Effect of $[K]_o$ on DF_{max}. A4. Both MDP and dV/dt_{max} measured during rotor activity were consistent predictors of rotor drift for all $[K]_o$ levels. B. Investigating the effect of changes in I-V relationship of I_{K1} resulting from altering its isoforms. B1. I_{K1} I-V profiles for a typical Kir2.1 and Kir2.3 dominant isoforms. B2. As in panel A2, rotor is drifting toward the excitability sink (lowest h×j) in the PV edge for any I-V profile. B3. Effect of the different I-V profiles in B1 on DF_{max} is small. B4. Both MDP and dV/dt_{max} measured during rotor activity were consistent predictors of rotor drift for all I-V profiles tested.

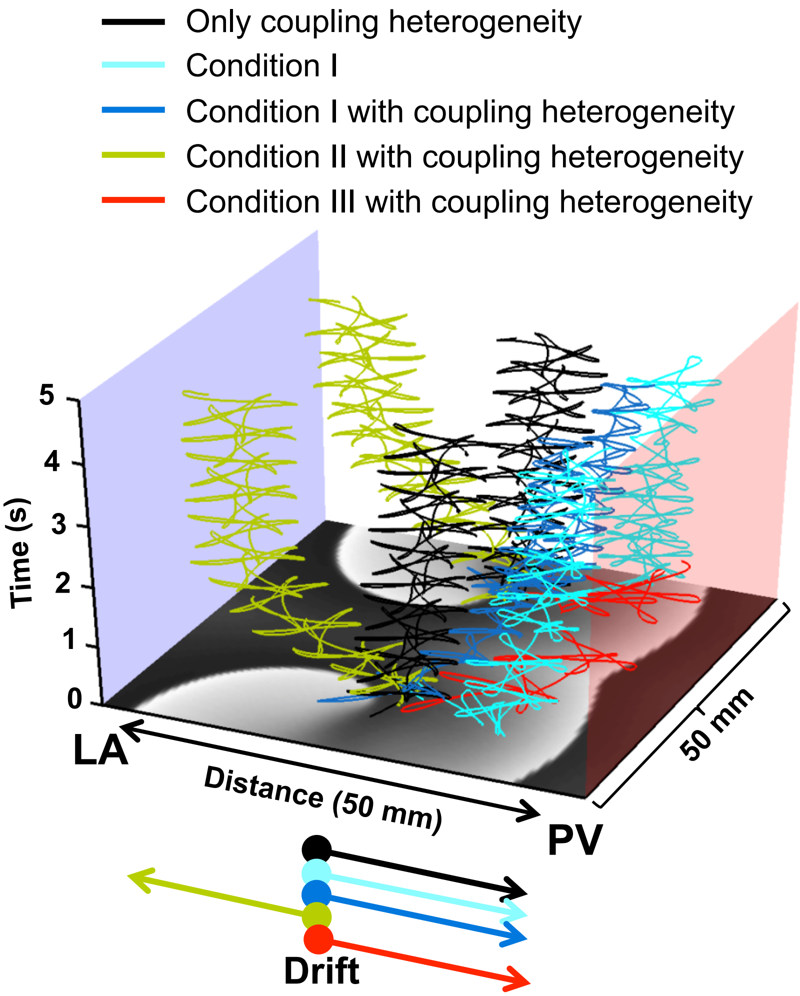

Fig. S7. Heterogeneous intercellular coupling in the PV-LAJ and rotor drift. Models were generated with heterogeneous isotropic intercellular coupling following a Boltzmann profile with 25% reduction in the PV vs. the LA edges. The figure shows a TSP and drift directions of counter-rotors at the various conditions indicated. In the presence of only coupling heterogeneity the rotors drift toward the PV (black) less than the drift with all ionic gradients (Cyan, Condition I). The drifts in the models with heterogeneous coupling combined with either Conditions I, II and III did not differ qualitatively from those with a uniform coupling (see Fig. 2) suggesting that the presence of the heterogeneous coupling does not alter the major role of I_{K1} in determining the rotor drift direction in the PV-LAJ toward the PV edge, where the coupling coefficient is lowest.

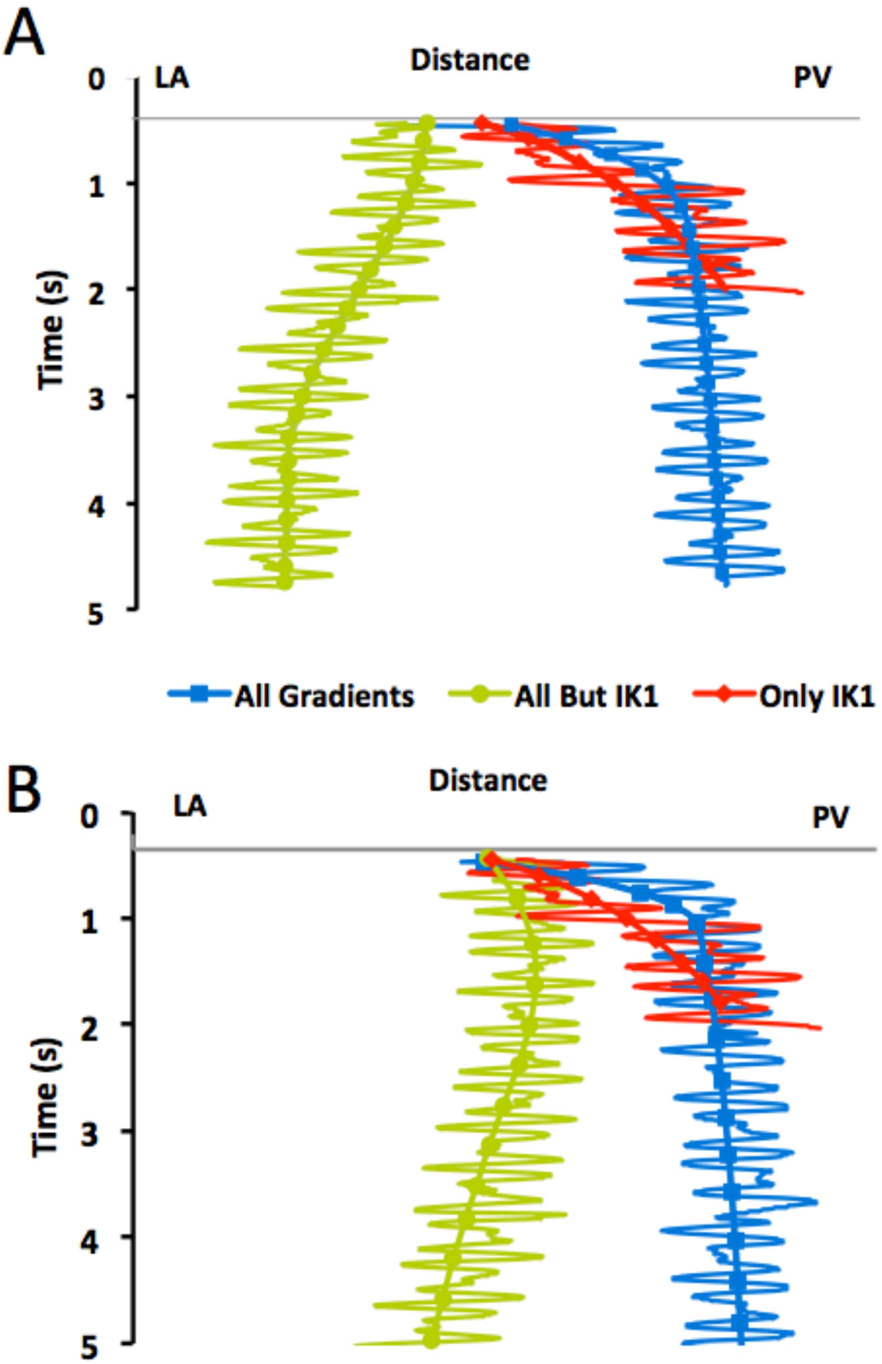

Fig. S8. Rotor drift in the presence of additional gradient in sodium current. The presence of I_{Na} gradients in the PV-LAJ is suspected but not yet confirmed. Thus we investigate its role in determining drift direction relative to I_{K1} gradient role. Gradients in I_{Na} whereby the PV conductance was reduced by 20% (panel A) and 40% (panel B) were incorporated in models similar to those used in Fig. 2. The TSPs here show SP trajectory for the 2 conditions of gradients in all currents (All Gradients; Condition I + gradient in I_{Na}; blue traces) and gradients in all currents, but I_{K1} (All but I_{K1}; Condition II + gradient in I_{Na}; green traces), as well as the gradient only in I_{K1} (Condition III; Only I_{K1}; red traces). Both panels show evolution of the tip trajectories for the rotors similar to those presented in Fig. 2, demonstrating that while I_{Na} contributes to the drift of the rotors in the PV-LAJ, I_{K1} is still the dominant current whose gradient determines drift direction.

SUPPLEMENTAL REFERENCE LIST

1. Wozniak-Skowerska, I., M. Skowerski, A. Wnuk-Wojnar, A. Hoffmann, S. Nowak, A. Gola, M. Sosnowski, and M. Trusz-Gluza. 2011. Comparison of pulmonary veins anatomy in patients with and without atrial fibrillation: analysis by multislice tomography. Int. J. Cardiol. 146: 181-185.
2. Courtemanche, M., R. J. Ramirez, and S. Nattel. 1998. Ionic mechanisms underlying human atrial action potential properties: insights from a mathematical model. American Journal of Physiology-Heart and Circulatory Physiology 44: H301-H321.
3. Kneller, J., R. Zou, E. J. Vigmond, Z. Wang, L. J. Leon, and S. Nattel. 2002. Cholinergic atrial fibrillation in a computer model of a two- dimensional sheet of canine atrial cells with realistic ionic properties. Circ. Res. 90: E73-E87.
4. Pandit, S. V., O. Berenfeld, J. M. Anumonwo, R. M. Zaritski, J. Kneller, S. Nattel, and J. Jalife. 2005. Ionic determinants of functional reentry in a 2-D model of human atrial cells during simulated chronic atrial fibrillation. Biophys. J. 88: 3806-3821.
5. Dhamoon, A. S., S. V. Pandit, F. Sarmast, K. R. Parisian, P. Guha, Y. Li, S. Bagwe, S. M. Taffet, and J. M. Anumonwo. 2004. Unique Kir2.x properties determine regional and species differences in the cardiac inward rectifier K+ current. Circ. Res. 94: 1332-1339.
6. Clayton RH, Zhuchkova E.A., Panfilov AV. 2005. Phase singularities and filaments: Simplifyingg complexity in computational models of ventricular fibrillation. Progress in Biophysics and Molecular Biology 90 (2006) 378-398
7. Cha, T. J., J. R. Ehrlich, L. Zhang, D. Chartier, T. K. Leung, and S. Nattel. 2005. Atrial Tachycardia Remodeling of Pulmonary Vein Cardiomyocytes: Comparison With Left Atrium and Potential Relation to Arrhythmogenesis. Circulation 111: 728-735.
8. Chaldoupi, S. M., P. Loh, R. N. Hauer, J. M. de Bakker, and H. V. van Rijen. 2009. The role of connexin40 in atrial fibrillation. Cardiovasc. Res. 84: 15-23.
9. Verhuele S, Wilson EE, Arora R., Engle SK., Scott LR., Olgin JE 2002. Tissue structure and connexin expression of canine pulmonary veins. Cardiovasc. Res. 55: 727-738.
10. Zlochiver, S., M. Yamazaki, J. Kalifa, and O. Berenfeld. 2008. Rotor meandering contributes to irregularity in electrograms during atrial fibrillation. Heart Rhythm 5: 846-854.
11. Zlochiver, S., V. Munoz, K. L. Vikstrom, S. M. Taffet, O. Berenfeld, and J. Jalife. 2008. Electrotonic myofibroblast-to-myocyte coupling increases propensity to reentrant arrhythmias in two-dimensional cardiac monolayers. Biophys. J 95: 4469-4480.
12. Noujaim, S. F., S. V. Pandit, O. Berenfeld, K. Vikstrom, M. Cerrone, S. Mironov, M. Zugermayr, A. N. Lopatin, and J. Jalife. 2007. Up-regulation of the inward rectifier K+ current (I K1) in the mouse heart accelerates and stabilizes rotors. J. Physiol 578: 315-326.
13. Hou, L., M. Deo, P. Furspan, S. V. Pandit, S. Mironov, D. S. Auerbach, Q. Gong, Z. Zhou, O. Berenfeld, and J. Jalife. 2010. A major role for HERG in determining frequency of reentry in neonatal rat ventricular myocyte monolayer. Circ. Res. 107: 1503-1511.
14. Campbell, K., C. J. Calvo, S. Mironov, T. Herron, O. Berenfeld, and J. Jalife. 2012. Spatial gradients in action potential duration created by regional magnetofection of hERG are a substrate for wavebreak and turbulent propagation in cardiomyocyte monolayers. J. Physiol 590: 6363-6379.

15. Warren, M., P. K. Guha, O. Berenfeld, A. Zaitsev, J. M. B. Anumonwo, A. S. Dhamoon, S. Bagwe, S. M. Taffet, and J. Jalife. 2003. Blockade of the inward rectifying potassium current terminates ventricular fibrillation in the guinea pig heart. J. Cardiovasc. Electrophysiol. 14: 621-631.
16. Samie, F. H., O. Berenfeld, J. Anumonwo, S. F. Mironov, S. Udassi, J. Beaumont, S. Taffet, and J. Jalife. 2001. Rectification of the Background Potassium Current: A Determinant of Rotor Dynamics in Ventricular Fibrillation. Circ Res 89: 1216-1223.
17. Ehrlich, J. R., T. J. Cha, L. M. Zhang, D. Chartier, P. Melnyk, S. H. Hohnloser, and S. Nattel. 2003. Cellular electrophysiology of canine pulmonary vein cardiomyocytes: action potential and ionic current properties. Journal of Physiology-London 551: 801-813.
18. Cha, T. J., J. R. Ehrlich, L. Zhang, D. Chartier, T. K. Leung, and S. Nattel. 2005. Atrial Tachycardia Remodeling of Pulmonary Vein Cardiomyocytes: Comparison With Left Atrium and Potential Relation to Arrhythmogenesis. Circulation 111: 728-735.